J. Fluid Mech. (2013), *vol.* 733, *pp.* 439–472.
doi:10.1017/jfm.2013.440

Stall onset on aerofoils at low to moderately high Reynolds number flows

Wallace J. Morris II and Zvi Rusak†

Department of Mechanical, Aerospace, and Nuclear Engineering Rensselaer Polytechnic Institute, Troy, NY 12180-3590, USA

(Received 13 March 2012; revised 11 August 2013; accepted 16 August 2013; first published online 24 September 2013)

The inception of leading-edge stall on stationary, two-dimensional, smooth, thin aerofoils at low to moderately high chord Reynolds number flows is investigated by a reduced-order, multiscale model problem via numerical simulations. The asymptotic theory demonstrates that a subsonic flow about a thin aerofoil can be described in terms of an outer region, around most of the aerofoil's chord, and an inner region, around the nose, that asymptotically match each other. The flow in the outer region is dominated by the classical thin aerofoil theory. Scaled (magnified) coordinates and a modified (smaller) Reynolds number (Re_M) are used to correctly account for the nonlinear behaviour and extreme velocity changes in the inner region, where both the near-stagnation and high suction areas occur. It results in a model problem of a uniform, incompressible and viscous flow past a semi-infinite parabola with a far-field circulation governed by a parameter $\tilde{A}$ that is related to the aerofoil's angle of attack, nose radius of curvature, thickness ratio, and camber. The model flow problem is solved for various values of $\tilde{A}$ through numerical simulations based on the unsteady Navier–Stokes equations. The value $\tilde{A}_s$ where a global separation zone first erupts in the nose flow, accompanied by loss of peak streamwise velocity ahead of it and change in shedding frequency behind it, is determined as a function of Re_M. These values indicate the stall onset on the aerofoil at various flow conditions. It is found that $\tilde{A}_s$ decreases with Re_M until some limit Re_M ($\sim$300) and then increases with further increase of Reynolds number. At low values of Re_M the flow is laminar and steady, even when stall occurs. The flow in this regime is dominated by the increasing effect of the adverse pressure gradient, which eventually overcomes the ability of the viscous stress to keep the boundary layer attached to the aerofoil. The change in the nature of stall at the limit Re_M is attributed to the appearance of downstream travelling waves in the boundary layer that shed from the marginal separation zone and grow in size with either $\tilde{A}$ or Re_M. These unsteady, convective vortical structures relax the effect of the adverse pressure gradient on the viscous boundary layer to delay the onset of stall in the mean flow to higher values of $\tilde{A}_s$. Computed results show agreement with marginal separation theory at low Re_M and with available experimental data at higher Re_M. This simplified approach provides a universal criterion to determine the stall angle of stationary thin aerofoils with a parabolic nose.

Key words: aerodynamics, boundary layers, boundary layer separation

† Email address for correspondence: rusakz@rpi.edu

1. Introduction

The term 'stall' of aerofoils refers to the significant loss of lift at a certain angle of attack (known as the stall angle) and above. This phenomenon results from the global (massive) separation of the flow along the aerofoil's upper surface due to interplay between viscous effects and adverse pressure gradients. Stall limits the lift of the aerofoil to a maximum value and thereby reduces the operational envelope of devices employing aerofoils.

Experimental studies of aerofoil stall at various Reynolds number flows are given in the classical investigations of Jones (1934), Jacobs & Sherman (1937), Abbott & von Doenhoff (1958) and Tani (1964), and the modern works by Selig *et al.* (1996) and Yen & Huang (2009). The experimental data provide the stall angle of attack for many aerofoils with various geometries. The stall angle is a function of chord Reynolds number (Re) and aerofoil geometry. Stall angle increases with Re for $Re > 100\,000$. The experimental measurements also show the existence of hysteresis loops between attached and globally separated flow states at angles of attack near stall when $Re > 100\,000$ (McCormick 1995, pp. 141–146). The range of angles of attack for these loops also increases with Re. On the other hand, at relatively low Re ($Re < 10\,000$) this behaviour becomes undetectable and the nature of stall may change. For example, the numerical computations of Kunz & Kroo (2001) show that the decrease of Re results in a higher stall angle.

There are two types of stall phenomenon on stationary aerofoils: see, for example, Anderson (2007), pp. 368–379 and the flow pictures of Ito shown in Nakayama (1988). The first is *leading-edge stall*, which characterizes relatively thin aerofoils with thickness ratios up to 15 % of the aerofoil's chord. Here, the flow separation zone evolves from the nose as the angle of attack is increased and the loss of suction around the nose and of lift is rather rapid and abrupt. The second type of stall is *trailing-edge stall*, which characterizes relatively thick aerofoils with thickness ratio above 15 % where the flow separation zone develops gradually from the trailing edge as the angle of attack is increased. Here the loss of suction and lift is gradual. In addition, impulsive starts or sinusoidal pitching motions of an aerofoil to high angles of attack result in unsteady leading-edge flow separation, formation of recirculating convective eddies, and loss of lift which depends on both the aerofoil's motion (pitch rate and location of centre of pitch) and the flow's complicated dynamics (shedding frequencies and size of eddies). This is known as the *dynamic stall* phenomenon (Bhaskaran & Rothmayer 1998; Carr 1988).

In the present paper we focus solely on the mechanism of the onset of the leading-edge stall on a stationary aerofoil in a uniform and incompressible steady flow with no background turbulence. Hereafter, reference to stall means leading-edge stall.

The experimental studies by Pavelka & Tatum (1981) demonstrate that leading-edge stall is preceded by the appearance of a 'short' recirculation bubble in the boundary layer at a much lower angle of attack. For low Reynolds number, $Re < 20\,000$, the flow is laminar and the short bubble grows with angle of attack and eventually bursts into a 'long' laminar separation zone causing the stall of the aerofoil (with transition to turbulence only far downstream in the separated flow region). In an intermediate range, $30\,000 < Re < 300\,000$ (upper limit depends on the thickness ratio), the burst of the laminar separation bubble still dominates the aerofoil's stall. However, in this range it is accompanied by a transition to flow unsteadiness and formation of convective vortical eddies and turbulence at pre-stall states. For higher Reynolds numbers, $Re > 500\,000$, the short bubble causes immediate transition to a turbulent boundary layer, which is less susceptible to adverse pressure gradients, keeping the

bubble size very small (less than 1 % of the aerofoil's chord). As the angle of attack is increased, the bubble size decreases, the adverse pressure gradient becomes more severe, the turbulent boundary layer separates, and the aerofoil stalls.

Theoretical studies of the leading-edge separation at the nose of an aerofoil were presented by Werle & Davis (1972), Cebeci, Khattab & Stewartson (1980), Cheng & Smith (1982), Ruban (1982) and Stewartson, Smith & Kaups (1982). Werle & Davis (1972) numerically solved the classical boundary-layer equations for an incompressible flow past a parabola at angle of attack. The inviscid solution of the velocity field on the parabola surface was prescribed as the outer velocity of the boundary layer. It was found that the shear stress vanishes along the parabola surface and a Goldstein-type singularity of the stress and the boundary-layer thickness are displayed when the vertical displacement of the stagnation point on the parabola exceeds a certain critical value, $K > 1.157$, which is independent of the flow Reynolds number. Cebeci *et al.* (1980) and Stewartson *et al.* (1982) found a similar result for $K > 1.155$. This value corresponds to a local pressure gradient parameter β below -0.2 (which also characterizes the separation of a laminar boundary layer on a flat plate under an adverse pressure gradient). Note that, according to our analysis, the matching of the parabola flow with the classical solution of the thin aerofoil theory (which satisfies the Kutta condition at the trailing edge) requires that $K = \alpha/\sqrt{R_c/2c}$ (here α is the angle of incidence, c is the aerofoil's chord, and R_c is the aerofoil's nose radius of curvature). This means that a necessary condition for onset of nose separation is $\alpha > \alpha_c = 1.157\sqrt{R_c/2c}$. However, this condition is not sufficient. The approach of Werle & Davis (1972) is limited to no interaction between the boundary-layer flow and the imposed outer flow; thereby it forces the singularity of the shear stress and can not accurately describe the structure of a separated flow state. Hence, it results in too low a prediction of the angle α_c for the onset of separation with respect to experimental findings (Jacobs & Sherman 1937; Abbott & von Doenhoff 1958; Selig *et al.* 1996).

An elegant asymptotic analysis of steady nose flow was conducted by Stewartson *et al.* (1982); see also a similar analysis by Ruban (1982). This analysis extended the Werle & Davis (1972) approach and resulted in a triple-deck theory of the steady boundary-layer flow about the separation point, also known as the marginal separation theory (MST). This approximation used a base velocity profile which is on the verge of separation and allowed an interaction between the inner, nearly separated flow close to the wall, and the outer inviscid flow around the separation point. The scales of the flow parameters in a local region around the separation point and its power law dependence on a modified Reynolds number Re_M based on R_c, $Re_M = UR_c/\nu$, were identified. An integral model equation was constructed for the solution of the flow structure near the wall and its relationship to the pressure changes in the outer flow. Computed results showed that attached-flow states exist when β ($=K$ in Werle & Davis 1972) is slightly greater than $\beta_c = 1.157$. For $\beta = \beta_c + m\Gamma(Re_M)^{-2/5}$, where m is a positive number, short closed separation bubbles appear when $\Gamma > 2.4$. The bubble grows in size until $\Gamma = \Gamma_c \approx 2.75$, where a fold in the solution branch occurs and larger closed separation bubbles are found for a certain range of $\Gamma < \Gamma_c$ as Γ is decreased from Γ_c. For $\Gamma > \Gamma_c \approx 2.75$ no solution of the model equation was found, suggesting that no steady separated flow can exist under these conditions and the bursting of the separation bubble and stall when the angle of attack is greater than $\alpha_s = [\beta_c + m\Gamma_c(Re_M)^{-2/5}]\sqrt{R_c/2c}$. Sychev *et al.* (1998, p. 174) stated that 'the oscillation in the flow under consideration was found to branch off from the steady solution in the domain of subcritical values of the *Re*. Typical of such flows is a subcritical type of transition to turbulence.' Also, Elliott & Smith (1987), working on

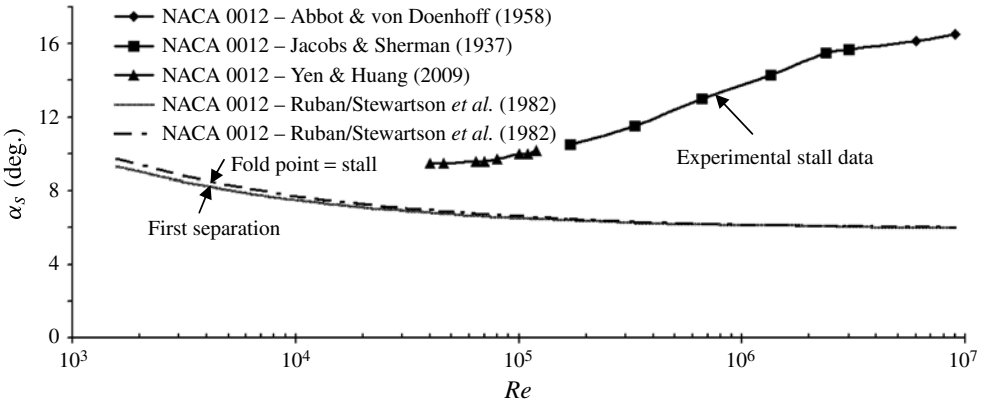

FIGURE 1. Current state of the art of stall prediction. MST predictions for first separation and for stall of a NACA 0012 wing section are compared with various available experimental stall points.

the unsteady marginal separation theory, found that perturbations of the steady solution are not damped in the course of time. On the contrary, a finite-time singularity appears in the unsteady solution, the van Dommelen & Shen (1980) singularity, which suggests the appearance of a major change in the flow.

The triple-deck approximation is limited in scope and describes only pre-stall states with marginal separation, not stall states with massive separation. It is also limited to a local region around the separation point which decreases in size with increase of Re_M and does not allow complete interaction between the separation zone and the accelerating flow around the leading edge, ahead of the separation. Therefore, it cannot describe the change of peak suction (streamwise velocity) or of wall shear stress in the boundary layer ahead of the separation bubble that may appear when eruption of the bubble occurs with the increase of angle of attack. The loss of peak suction is an important characteristic of stall. Moreover, identification of stall based on lack of solutions of the limited steady MST model equation or on a finite-time singularity in the unsteady triple-deck approximation is only a mathematical indication that a major change may occur in the flow which the approximations cannot capture. These mathematical properties cannot be used as a stand-in for identifying the appearance of a physical phenomenon that must be measured by changes in physical flow parameters.

In addition, Sychev *et al.* (1998, p. 172) summarized the results from steady MST and presented formulae for the first appearance of a short separation bubble at $\alpha' = \alpha'_0(1 + 2.037Re_M^{-2/5} + \cdots)$ and then its bursting (stall) at $\alpha_s = \alpha'_0(1 + 2.376Re_M^{-2/5} + \cdots)$, where $\alpha'_0 = 0.8172\delta$ (δ is the aerofoil's relative thickness). The formulae of Sychev *et al.* (1998) are used in figure 1 to demonstrate MST's prediction of the first separation angle (solid line) and stall angle (dot-dashed line) as a function of Re for the NACA 0012 aerofoil. Also shown in figure 1 are experimental points of stall angle α_s of the NACA 0012 aerofoil as taken from data in Jacobs & Sherman (1937), Abbott & von Doenhoff (1958) and Yen & Huang (2009). Currently, no data are found for flows with $Re < 40\,000$ or $Re > 10$ million. The figure exhibits a disparity between the MST predictions and the results measured from experiments. Moreover, the theory predicts that stall angle decreases with Re while the experiments show the opposite trend when $Re > 40\,000$.

Moreover, both numerical simulations by Kunz & Kroo (2001) and experiments by Yen & Huang (2009) show the first appearance of short closed separation bubbles near the aerofoil's nose at low angles of attack which are accurately predicted by MST. However, the experiments of Yen & Huang (2009) show for the case of the NACA 0012 at $Re > 40\,000$ that the flow continues to maintain a globally attached state around most of the aerofoil at a wide range of higher angles of attack, and stall occurs only when massive separation erupts at an angle that is higher than that predicted by MST. For example, at $Re = 46\,000$, the leading-edge bubble appears at $\alpha = 6^\circ$ (MST prediction gives $\alpha_s = 6.6^\circ$) while stall occurs at $\alpha = 10^\circ$. Therefore, MST prediction is limited to the appearance of the first separation at low Re, but cannot predict the nature of the flow and stall at the higher Reynolds numbers (see figure 1).

Despite being a basic and classical phenomenon in aerodynamics that limits the envelope of aerofoil operation, the onset of stall on stationary aerofoils and its mechanism is not yet fully understood. To the best of our knowledge, there is no theoretical approach that can yet accurately predict the stall angle of practical aerofoils as a function of the flow Reynolds number.

In a recent paper (Rusak & Morris 2011) we studied the leading-edge stall of thin aerofoils at subsonic speeds and moderately high Reynolds numbers, and we accounted for the interactions between the near-wall viscous flow and the outer inviscid flow. The analysis resulted in a model (simplified) problem of a uniform, compressible, steady stream at Re_M past a semi-infinite, stationary, canonic parabola with a far-field circulation governed by a parameter $\tilde{A}$. This parameter is related to the angle of attack, nose radius of curvature, and camber of the aerofoil and to flow Mach number. The model parabola problem was solved numerically using the Reynolds-averaged Navier–Stokes (RANS) formulation, and results were used to determine the value $\tilde{A}_s$ where a large separation zone first appears in the nose flow concurrent with a sudden drop of the maximum suction. The change of $\tilde{A}_s$ with Re_M was computed. Predicted stall angles and maximum lift values showed agreement with results from much of the available experimental data for various aerofoil geometries at chord Reynolds numbers $Re > 40\,000$ (corresponding to nose Reynolds number $Re_M > 700$ for a NACA 0012 wing section).

This paper extends the model problem in Rusak & Morris (2011) to investigate the onset of leading-edge stall on stationary, thin aerofoils at low to moderately high Reynolds numbers (Re_M in the range 50 to 2100). This work also seeks to illuminate the flow physics in this range as well as establish an overlap region with the previously investigated stall at moderately high to high Re_M. Numerical simulations based on the unsteady, incompressible Navier–Stokes equations of a viscous flow around a semi-infinite, stationary, canonic parabola are conducted. These simulations are used to determine the value $\tilde{A}_s$ as a function of Re_M. Computed results are compared with MST predictions and available experimental data and shed light on the gap witnessed in figure 1 between theory and experiments.

2. Theoretical study

We consider a stationary, thin and smooth aerofoil whose geometry is given by $y = \delta c F_{u,l}(x/c)$ for $0 \leqslant x \leqslant c$, where c is the chord. The upper and lower surface shape functions $F_{u,l}(x/c)$ are described by $F_{u,l}(x/c) = C_a(x/c) \pm 0.5t(x/c)$ with thickness ratio $0 < \delta \ll 1$. Here, $C_a(x/c)$ is the camber-line function, $t(x/c)$ is the thickness function and the aerofoil's nose is parabolic with a radius of curvature $R_c = 2\delta^2 h^2 c$ (h is called the nose curvature parameter). It should be noted that, for subsonic applications, nearly

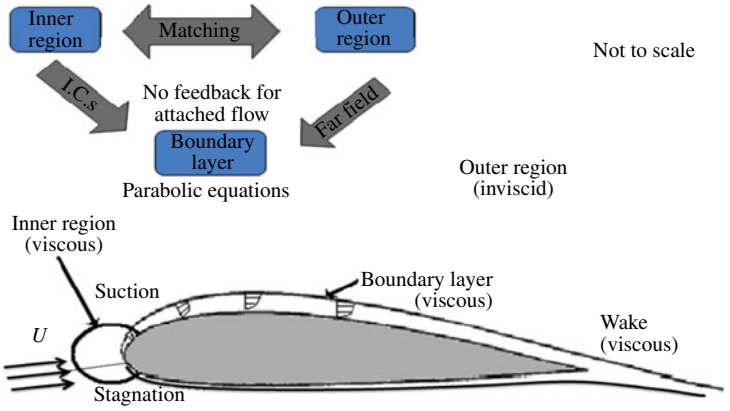

FIGURE 2. (Colour online) The physical model and various regions considered.

all aerofoils have parabolic nose geometry (see Abbott & von Doenhoff 1958). This aerofoil is given in a uniform, steady, incompressible upstream flow with constant speed U_∞ along the x-axis, chord Reynolds number $Re = \rho U_\infty c/\mu \gg 1$, at low to moderately high angle of attack α (up to the stall angle α_s), and with no background turbulence. Here ρ and μ are respectively the constant density and viscosity of the flow. We introduce $A = \alpha/\delta$. We also assume that Re is sufficiently high such that $Re_M = ReR_c/c \gg 1$.

The flow field around the aerofoil involves several length scales, and an analytical solution of this flow problem is beyond reach. We offer a simplified physical model for the attached flow around the aerofoil: see figure 2. A basic representation of the flow is composed of a small inner region around the aerofoil's parabolic nose and an outer region around the rest of the aerofoil. In the inner region the flow is characterized by large changes resulting from a stagnation point on the lower surface and flow acceleration around the nose to a maximum speed (minimum pressure) point on the upper surface. In the outer region the flow develops with smaller changes from the uniform free stream. The lower and upper thin, viscous boundary layers that are attached to the aerofoil surfaces begin at the stagnation point in the inner region and develop through the outer region, separating near the trailing edge into the viscous wake (note: in figure 2 the boundary layers and wake are not drawn to scale, but are enlarged for demonstration purposes). Moreover, the far field of the inner region matches the near-nose behaviour of the flow in the outer region, specifically outside the boundary layers. The thin boundary layers initiated inside the inner region provide (as they develop into the outer region) the upstream conditions for the outer region's thin boundary layer. The outer region's near-aerofoil, inviscid behaviour of the velocity and pressure provide the far-field conditions for the boundary layer.

The attached thin boundary layer of the outer region slightly modifies the potential flow around the aerofoil via the Kutta condition at the trailing edge. Any effect due to this interaction is likely to become more significant at higher angles of attack, specifically when flow separation occurs near the trailing edge. In this study such effects of trailing-edge separation are assumed to have a small influence on the inner flow behaviour leading to stall and are excluded. Therefore, in this approach, the boundary-layer solution in the outer region is not needed for the purpose of computing

the flow around the leading edge. However, the development of the boundary layer within the inner region is strongly affected by the behaviour of the flow in the outer region surrounding the nose (which is the far field of the inner region). Therefore, an accurate matching between the solutions of the inner and outer regions outside the boundary layer is needed: see figure 2. Further, a complete interaction in all directions (space and time) between this viscous boundary layer and the inner flow around the nose must be considered as a whole.

Ultimately, this model allows a reduction of the nose flow to a flow in rescaled coordinates with a rescaled Reynolds number (Re_M) around a stationary canonic parabola whose far field is dictated by the steady, inviscid, near-nose behaviour of the full aerofoil geometry, as estimated from the thin aerofoil theory. This allows for magnifying the flow behaviour near the nose and capturing the stall onset. The onset of the leading-edge stall on an aerofoil is then related to the sudden rupturing of the boundary layer on the parabola accompanied by a loss of peak suction ahead of the separation bubble and change of shedding frequency behind the separation bubble (when unsteady flow develops at certain Re_M). Numerical simulations are used to simulate the inner region flow at low to moderately high Re_M and to identify the angle for the onset of leading-edge stall on the entire aerofoil.

The present model allows for significant computational advantage through the rescaling of both geometry and Re. Attempting to resolve similar flow details for full geometry wing sections requires an extremely dense mesh around the section nose, resulting in the need for adaptive mesh techniques (Webster *et al.* 1994), the computational cost of which is still much higher.

In the Appendix we develop detailed asymptotic expansions of the velocity components in the outer region around most of the aerofoil and in an inner region near the nose, in terms of the aerofoil's small thickness ratio δ and angle of attack α. We also formulate the matching between these expansions. The analysis shows that the inner-region flow is described by a reduced-order model problem. This problem consists of an incompressible and viscous flow around a canonic parabola described by (A 7) and (A 8), which is governed by the no-slip and no-penetration conditions along the parabola surface, and by the steady far-field behaviour given by (A 9) where the circulation parameter is $\tilde{A} = Aw_0/h$. The circulation parameter $\tilde{A}$ of the inner problem is dictated by the aerofoil's geometry and angle of attack. We also conclude from the matching that for the study of leading-edge stall over thin aerofoils we can focus solely on the inner region problem where the increasing adverse pressure gradient on the upper surface of the parabola is directly related to the increase of $\tilde{A}$. The increase in adverse pressure gradient acts against the attached viscous boundary layer and eventually causes massive separation and stall. The error in the matching is of the order of $O(\delta^2, \alpha^2)$. For thin aerofoils of practical interest with $\delta < 0.15$ and $|\alpha| < 15^\circ$ the error of matching is less than a few per cent.

2.1. *Stall prediction*

In the present work, we look for the specific values of $\tilde{A}$ as a function of Re_M, i.e. $\tilde{A}_s(Re_M)$, at which there occurs a sudden rupturing of the boundary. This indicates a sufficient condition for the onset of leading-edge stall on aerofoils: $\tilde{A} > \tilde{A}_s(Re_M)$. In this sense, the present results are universal. From the values of $\tilde{A}_s$ we can predict the angle of stall of an aerofoil at a given Reynolds number. Note that the circulation parameter is $\tilde{A} = (\alpha - \delta\bar{w}_0)/\delta h = (\alpha - \alpha_{0l} - \delta\bar{w}_1/2)/\sqrt{R_c/2c}$ and then the predicted angle of stall and maximum lift coefficient are given by (see also

Rusak & Morris 2011):

$$\alpha_s = \tilde{A}_s\sqrt{\frac{R_c}{2c}} + \alpha_{0l} + \delta\frac{\bar{w}_1}{2} = \tilde{A}_s\sqrt{\frac{R_c}{2c}} + \delta\bar{w}_0 \tag{2.1a}$$

and

$$C_{l\,max} = 2\pi\,(\alpha_s - \alpha_{0l}) = 2\pi\tilde{A}_s\sqrt{\frac{R_c}{2c}} + \pi\delta\bar{w}_1. \tag{2.1b}$$

Here we used the relationship $\delta h = \sqrt{R_c/2c}$. Also note that according to the thin aerofoil theory the aerofoil's lift coefficient is $C_l = 2\pi(\alpha - \alpha_{0l})$, where the zero lift angle is given by $\alpha_{0l} = \delta(\bar{w}_0 - \bar{w}_1/2)$ and

$$\bar{w}_0 = \frac{1}{\pi A}\int_0^\pi \frac{\mathrm{d}C_a}{\mathrm{d}\bar{x}}\,(\vartheta)\;\mathrm{d}\vartheta, \quad \bar{w}_1 = \frac{2}{\pi A}\int_0^\pi \frac{\mathrm{d}C_a}{\mathrm{d}\bar{x}}\,(\vartheta)\cos\vartheta\;\mathrm{d}\vartheta, \tag{2.2}$$

where $\bar{x} = x/c = (1-\cos\vartheta)/2$. Formulae (2.1*a*) and (2.1*b*) provide predictions of order $O(\delta, \alpha)$ and the expected error is $O(\delta^2, \alpha^2)$. This means that the theory is limited to aerofoils with small thickness ratio, and as the thickness increases the error of this prediction also increases. Our numerical studies, presented in Rusak & Morris (2011), indicate that for practical aerofoils the theory provides relevant predictions when $\delta < 0.15$ and $|\alpha_s| < 15°$.

3. Numerical simulation of parabola (inner) problem

The two-dimensional, viscous, incompressible and unsteady Navier–Stokes equations for the inner flow around a canonic parabola are

$$\frac{\partial u}{\partial x} + \frac{\partial v}{\partial y} = 0, \tag{3.1a}$$

$$\frac{\partial u}{\partial t} + u\frac{\partial u}{\partial x} + v\frac{\partial u}{\partial y} = -\frac{\partial p}{\partial x} + \frac{1}{Re_M}\nabla^2 u, \tag{3.1b}$$

$$\frac{\partial v}{\partial t} + u\frac{\partial v}{\partial x} + v\frac{\partial v}{\partial y} = -\frac{\partial p}{\partial y} + \frac{1}{Re_M}\nabla^2 v. \tag{3.1c}$$

With respect to the Appendix equations, stars are removed for simplicity. Using the vorticity–streamfunction approach, we define the axial and the normal velocities and the vorticity by the following equations:

$$u = \frac{\partial\psi}{\partial y}, \quad v = -\frac{\partial\psi}{\partial x} \quad \text{and} \quad \omega = \frac{\partial v}{\partial x} - \frac{\partial u}{\partial y}. \tag{3.2}$$

This allows reduction of (3.1) to only two dependent variables and equations, namely the streamfunction and the vorticity respectively:

$$\frac{\partial\omega}{\partial t} + \frac{\partial\psi}{\partial y}\frac{\partial\omega}{\partial x} - \frac{\partial\psi}{\partial x}\frac{\partial\omega}{\partial y} = \frac{1}{Re_M}\nabla^2\omega, \tag{3.3a}$$

$$\frac{\partial^2\psi}{\partial x^2} + \frac{\partial^2\psi}{\partial y^2} = -\omega. \tag{3.3b}$$

Using the above definitions, u and v can then be computed once ψ and ω are solved, and then the pressure can be found using the equation

$$\nabla^2 p = -\left[\frac{\partial(u^2)}{\partial x^2} + 2\frac{\partial(uv)}{\partial x \partial y} + \frac{\partial(v^2)}{\partial y^2}\right]. \tag{3.4}$$

Equations (3.3) are subjected to the tangency and no-slip flow conditions on the canonic parabola surface and the far-field behaviour as described by (A 9).

Parabolic coordinates $x = (\mu^2 - \eta^2)/2$ and $y = \mu\eta$ are used to transform the field into a Cartesian computational space. Here μ is the coordinate parallel to the surface of the parabola and η is the coordinate normal to the surface. The canonic parabola is now described by the $\eta = 1$ surface, and flow evolves in the domain $-\infty < \mu < +\infty$, $\eta > 1$. In parabolic coordinates the velocity components can be given by

$$V_\mu = \frac{1}{\sqrt{\mu^2 + \eta^2}}\frac{\partial \psi}{\partial \eta}, \quad V_\eta = \frac{-1}{\sqrt{\mu^2 + \eta^2}}\frac{\partial \psi}{\partial \mu}. \tag{3.5}$$

Then, the Navier–Stokes equations (3.3) become

$$\frac{\partial \omega}{\partial t} + \frac{1}{(\mu^2 + \eta^2)}\left(\frac{\partial \psi}{\partial \eta}\frac{\partial \omega}{\partial \mu} - \frac{\partial \psi}{\partial \mu}\frac{\partial \omega}{\partial \eta}\right) = \frac{1}{Re_M}\frac{1}{\mu^2 + \eta^2}\left(\frac{\partial^2 \omega}{\partial \mu^2} + \frac{\partial^2 \omega}{\partial \eta^2}\right), \tag{3.6a}$$

$$\omega = \frac{-1}{\mu^2 + \eta^2}\left(\frac{\partial^2 \psi}{\partial \mu^2} + \frac{\partial^2 \psi}{\partial \eta^2}\right). \tag{3.6b}$$

The vorticity transport and streamfunction equations were rearranged to produce the following conservative form:

$$\frac{\partial \omega}{\partial t} + \frac{1}{\mu^2 + \eta^2}\left(\frac{\partial}{\partial \mu}\left(\sqrt{\mu^2 + \eta^2}V_\mu \omega\right) + \frac{\partial}{\partial \eta}\left(\sqrt{\mu^2 + \eta^2}V_\eta \omega\right)\right) = \frac{1}{Re_M(\mu^2 + \eta^2)}\left(\frac{\partial^2 \omega}{\partial \mu^2} + \frac{\partial^2 \omega}{\partial \eta^2}\right), \tag{3.7a}$$

$$\omega = \frac{-1}{\mu^2 + \eta^2}\left(\frac{\partial^2 \psi}{\partial \mu^2} + \frac{\partial^2 \psi}{\partial \eta^2}\right). \tag{3.7b}$$

Equations (3.7) are subjected to the tangency and no-slip flow conditions on the canonic parabola surface, i.e. $V_\eta(\mu, \eta = 1) = V_\mu(\mu, \eta = 1) = 0$, $\psi(\mu, \eta = 1) = 0$. Using the inversion of the coordinates transform,

$$\eta = \sqrt{\sqrt{x^2 + y^2} - x}, \quad \mu = \sqrt{\sqrt{x^2 + y^2} + x}, \tag{3.8}$$

it can be shown that the far-field behaviour as described by (A 9) results in $\Phi^* \approx (\mu^2 - \eta^2)/2 + \eta + \tilde{A}\mu$. In the far field, $V_\mu = (\mu + \tilde{A})/\sqrt{\mu^2 + \eta^2}$ and $V_\eta = (1 - \eta)/\sqrt{\mu^2 + \eta^2}$, from which

$$\psi = \mu\eta - \mu + \tilde{A}\eta \tag{3.9}$$

as both μ and η tend to infinity. Note that the far-field behaviour, when applied to the whole domain, is the inviscid, steady-state solution of the problem for all $\tilde{A}$.

For a numerical implementation, the semi-infinite domain $\eta \geqslant 1$, $-\infty < \mu < \infty$ is reduced to the computational domain $-\mu_{max} \leqslant \mu \leqslant \mu_{max}$ and $1 \leqslant \eta \leqslant \eta_{max}$, where μ_{max} and η_{max}, are sufficiently large. This domain is discretized by a uniform mesh with

constant step sizes in both directions $\Delta\mu$ and $\Delta\eta$, respectively. The index of each grid point is (i, j) respectively, where $-M \leqslant i \leqslant M$, $1 \leqslant j \leqslant N$. Time is discretized by constant time steps Δt with index n for each time level. The time derivative in (3.7*a*) is approximated by a first-order forward difference, and second-order central differences are used to approximate the spatial derivatives. The discretized formulation of (3.7*a*) is

$$\frac{\omega_{i,j}^{n+1} - \omega_{i,j}^{n}}{\Delta t} + \frac{1}{s_{i,j}^2}\left[\frac{s_{i+1,j}V_{\mu_{i+1,j}}^{n}\omega_{i+1,j}^{n} - s_{i-1,j}V_{\mu_{i-1,j}}^{n}\omega_{i-1,j}^{n}}{2\Delta\mu} + \frac{s_{i,j+1}V_{\eta_{i,j+1}}^{n}\omega_{i,j+1}^{n} - s_{i,j-1}V_{\eta_{i,j-1}}^{n}\omega_{i,j-1}^{n}}{2\Delta\eta}\right] = \frac{1}{Re_M s_{i,j}^2}\left[\frac{\omega_{i-1,j}^{n} - 2\omega_{i,j}^{n} + \omega_{i+1,j}^{n}}{(\Delta\mu)^2} + \frac{\omega_{i,j-1}^{n} - 2\omega_{i,j}^{n} + \omega_{i,j+1}^{n}}{(\Delta\eta)^2}\right], \tag{3.10}$$

where $s_{i,j} = \sqrt{\mu_{i,j}^2 + \eta_{i,j}^2}$. Equation (3.10) is rearranged to solve for $\omega_{i,j}^{n+1}$ in terms of the fields of vorticity and velocity at time level n. Once the vorticity field is progressed in time, the streamfunction at time level $n+1$ is solved using spatial central differences:

$$\frac{\psi_{i-1,j}^{n+1} - 2\psi_{i,j}^{n+1} + \psi_{i+1,j}^{n+1}}{(\Delta\mu)^2} + \frac{\psi_{i,j-1}^{n+1} - 2\psi_{i,j}^{n+1} + \psi_{i,j+1}^{n+1}}{(\Delta\eta)^2} = -\omega_{i,j}^{n+1}. \tag{3.11}$$

Equation (3.11) is solved by the Jacobi iteration method. Once convergence to a given tolerance is achieved, the velocity field at time level $n+1$ can be determined from

$$V_{\mu}^{n+1} = \frac{1}{\sqrt{\mu_{i,j}^2 + \eta_{i,j}^2}}\frac{\psi_{i,j+1}^{n+1} - \psi_{i,j-1}^{n+1}}{2\Delta\eta}, \quad V_{\eta}^{n+1} = \frac{-1}{\sqrt{\mu_{i,j}^2 + \eta_{i,j}^2}}\frac{\psi_{i+1,j}^{n+1} - \psi_{i+1,j}^{n+1}}{2\Delta\mu}. \tag{3.12}$$

Equations (3.10) and (3.11) are solved under the following conditions: (i) a wall boundary condition $\psi_{i,j=1}^{n} = 0$ for all $-M \leqslant i \leqslant M$; (ii) an inflow far field $\psi_{i,j=N}^{n}$, given by the far-field potential flow behaviour (3.9), and $\omega_{i,j=N}^{n} = 0$ are employed for $-M \leqslant i \leqslant M$; (iii) an outflow $\psi_{i=\pm M,j}^{n}$, given by the far-field flow behaviour (3.9), and $\omega_{i=\pm M,j}^{n} = 0$ are used for $N_{BL} \leqslant j \leqslant N$; (iv) a Neumann boundary condition $(\partial\psi/\partial\mu)_{i=\pm M,j}^{n} = (\partial\omega/\partial\mu)_{i=\pm M,j}^{n} = 0$ along the outflow boundaries $i = \pm M$ for $1 < j < N_{BL}$ which allows the outflow to evolve naturally (here $N_{BL} = N/20$ is used); (v) the vorticity $\omega_{i,j=1}^{n}$ (along the parabola surface $j = 1$) for $-M < i < M$ is computed by a second-order, forward difference approximation in the j direction, which also accounts for the wall no-slip condition along a stationary boundary (see details in Hoffmann & Chiang 1993), i.e. $\omega_{i,j=1}^{n} = (7\psi_{i,j=1}^{n} - 8\psi_{i,j=2}^{n} + \psi_{i,j=3}^{n})/2(\Delta\eta)^2$.

The computations are first-order accurate in time and second-order accurate in space, and are consistent with the original (3.7) as the mesh is refined. The field of velocity and vorticity at time level $n+1$ are used to advance the solution to the next time step. For a given Re_M and $\tilde{A}$, the solution of (3.10)–(3.12) is advanced in time until time-asymptotic behaviour, steady or periodic, is achieved.

The computations are initiated in the following way. At a given Re_M and $\tilde{A} = 0$ we start with the inviscid, potential flow solution as an initial state and march in time until a steady, time-asymptotic state of the viscous flow problem is found. Then, we use this solution as an initial state for the computation of the flow evolution at the same Re_M, with an increased incremental value of $\tilde{A}$ with essentially zero rate of change, for

example $\tilde{A} = 0.1$. Similarly, each time-asymptotic state is used as an initial state for computation of flow evolution at the next nearby value of $\tilde{A}$.

Certain numerical stability criteria must be satisfied in the computations. Here we require that the Courant–Friedrichs–Lewy (CFL) number C_k, diffusion number d_k, and the cell Reynolds number Re_C, that is,

$$C_k = a\frac{\Delta t}{\Delta x_k}, \quad d_k = \frac{1}{Re_M}\frac{\Delta t}{(\Delta x_k)^2}, \quad Re_c = \Delta x_k Re_M, \tag{3.13}$$

obey certain limitations. In the present numerical calculations, $a = U_{max} = 1$ and x_k indicates μ or η. Extending von Neumann numerical linear stability analysis (see chapter 4 of Hoffmann & Chiang 1993 and chapter 3 of Roache 1998) to the present forward-in-time, central-in-space differencing scheme leads to the following stability requirements in a two-dimensional problem: $C = C_\mu + C_\eta \leqslant 1, d = d_\mu + d_\eta \leqslant 1/2$, and $Re_C \leqslant 4/C$. For example, with $Re_M = 700$, $\Delta\mu = 0.2$ and $\Delta\eta = 0.025$, the CFL number dictates that Δt is less than 0.0222 and the diffusion number states that it must be less than 0.215, while the cell Reynolds number criterion ($\sim$141 in this case) calls for $\Delta t \leqslant 0.00063$. Clearly, for this case, the cell Reynolds number criterion is the most restrictive and is therefore used as the maximum threshold for Δt, dictating small time steps. Further, we refer to the work by Thompson, Webb & Hoffman (1985), later verified by Sousa (2003), which states that the cell Reynolds number restriction is overly restrictive for stable calculations. In spite of this fact, we proceed to use it as a buffer against numerical instabilities that may result from nonlinear effects. As a result, the CFL number is less than 0.01, which provides high accuracy of resolution of velocity signals in time, specifically of the low-frequency waves that are shed behind the separation bubble, convect along the parabola surface and are involved in the delay of stall at $Re_M > 300$.

4. Computed results

4.1. *Numerical convergence studies*

In the parabolic-coordinate computational space, we have an impinging uniform flow from the top of the domain that is modified by the far-field behaviour, which is governed by the circulation parameter. The flow runs over the plane $\eta = 1$ and splits into two streams that run out through either side of the domain. A representative computed field of streamlines for the steady flow case where $Re_M = 700$ and $\tilde{A} = 1.4$ is shown in figure 3. The surface $\eta = 1$ is the canonic parabola (see the inner region of figure 2) that has been 'unwrapped' to a flat wall via the mapping, with the leading edge at the centre ($\mu = 0$). Flow along the lower surface proceeds to the left while flow on the upper surface proceeds to the right. In most computations we used $\mu_{max} = 20$ and $\eta_{max} = 11$ (which represent a far field of 200 nose radii from the parabola leading edge in the physical domain). Note that the flow asymmetry about $\mu = 0$ exhibited in this figure results from the far-field effect through the parameter $\tilde{A}$.

We first conducted convergence studies of the numerical solutions with mesh refinement. In figure 4 we show results for a representative test case, where $Re_M = 100$ and $\tilde{A} = 0.0$ with four meshes: one mesh with $\Delta\mu = 0.8$ and $\Delta\eta = 0.025$ (50×400), the second with $\Delta\mu = 0.4$ and $\Delta\eta = 0.025$ (100×400), a third mesh with $\Delta\mu = 0.2$ and $\Delta\eta = 0.025$ (200×400), and a finer mesh with $\Delta\mu = 0.1$ and $\Delta\eta = 0.025$ (400×400). The results show time-asymptotic computed velocity V_μ along the line $\eta = 1.025$ (the closest grid line to the wall, being the most sensitive to changes in the

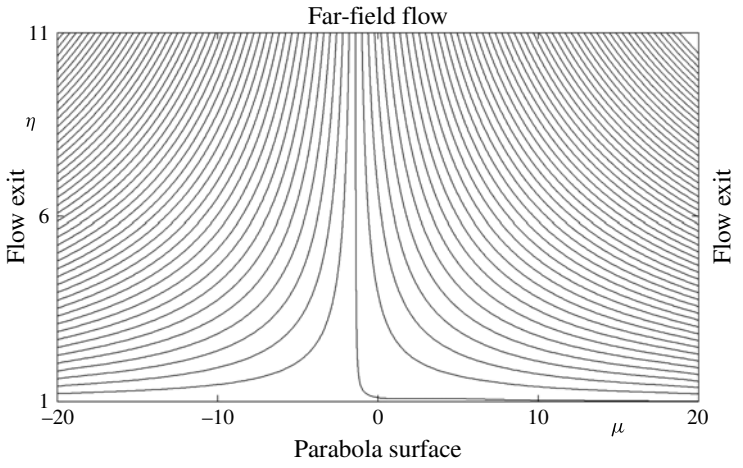

FIGURE 3. Representative field of streamlines in the computational domain for $Re_M = 700$ and $\tilde{A} = 1.4$.

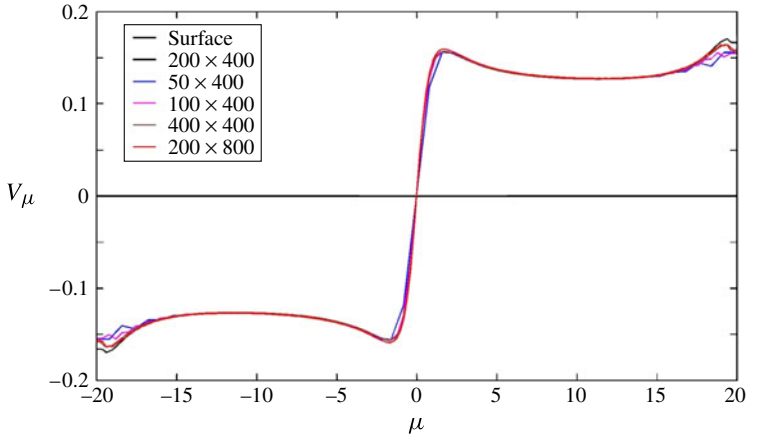

FIGURE 4. (Colour online) Mesh refinement study: $Re_M = 100$; $\tilde{A} = 0.0$; $\eta = 1.025$.

flow) from the four meshes. Results agree all along the line as the horizontal step $\Delta\mu$ is reduced, save for small variations near the domain edges. Similar agreement was found along all other grid lines η. Further, results for V_μ along the wall-adjacent grid line $\eta = 1.025$ from two meshes with $\Delta\mu = 0.2$ and $\Delta\eta = 0.0125$ (200×800) and $\Delta\mu = 0.2$ and $\Delta\eta = 0.025$ (200×400) also show agreement as the vertical step size $\Delta\eta$ is reduced. Similar convergence of computed results was found for all other values of Re_M and $\tilde{A}$, as long as the flow stayed attached. For example, the case $Re_M = 100$ and $\tilde{A} = 1.7$ along the grid lines $\eta = 1.025$ and 1.05 in figure 5(*a*,*b*), respectively, demonstrates mesh convergence of computed results at low Reynolds numbers and a state just prior to global separation. Similarly, convergence is found at a higher Reynolds number, $Re_M = 700$ and $\tilde{A} = 1.3$, shown in figure 6(*a*,*b*). It can be concluded that a mesh with $\Delta\mu = 0.2$ and $\Delta\eta = 0.025$ provides sufficiently converged solutions

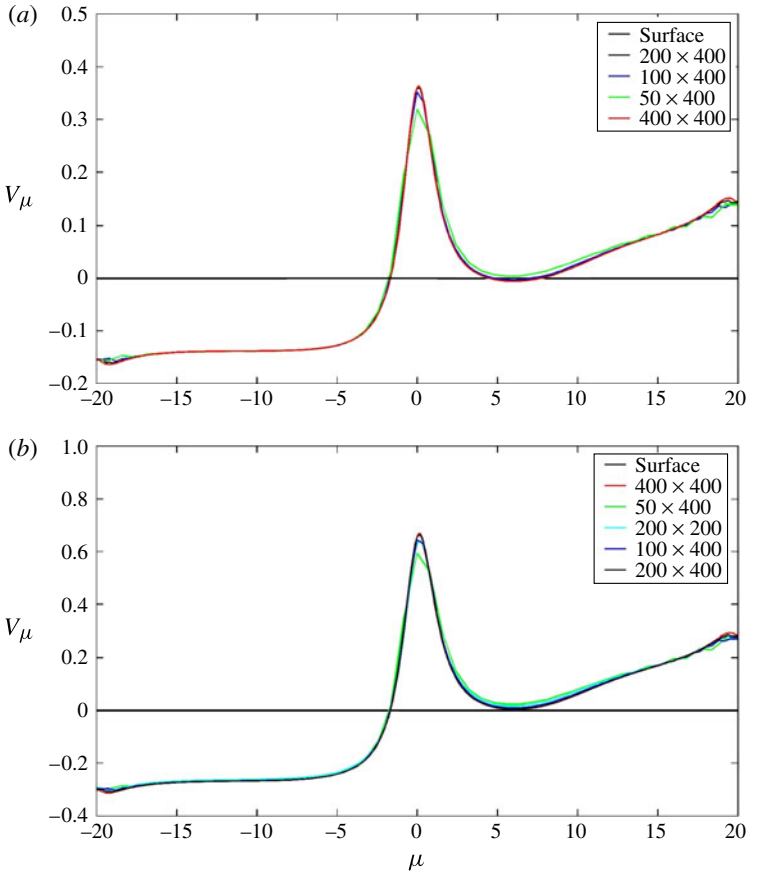

FIGURE 5. (Colour online) Mesh refinement study: $Re_M = 100$; $\tilde{A} = 1.7$; (*a*) $\eta = 1.025$, (*b*) $\eta = 1.05$.

for all steady flows with Re_M up to 700 (see additional cases in Morris 2009). Further convergence studies showed that smaller grid steps are needed for converged steady flow solutions at Re_M above 700.

In addition, at Re_M above a certain value (300) and at high values of $\tilde{A}$ (>1.3) the flow exhibits the shedding of natural unsteady eddies behind the separation bubble that convect along the upper surface of the stationary parabola while the flow remains globally attached. Such situations play a role in the stall mechanism and require additional mesh convergence studies to adequately resolve the velocity field and the spectral content of dominant eddies. Figure 7 presents an example of time-averaged streamwise velocity profiles for the case of $Re_M = 700$ and $\tilde{A} = 1.5$ along grid line $\eta = 1.025$ as computed from various meshes including $\Delta\mu = 0.2$ and $\Delta\eta = 0.025$ (200 × 400), $\Delta\mu = 0.1$ and $\Delta\eta = 0.025$ (400 × 400), $\Delta\mu = 0.05$ and $\Delta\eta = 0.025$ (800 × 400), $\Delta\mu = 0.025$ and $\Delta\eta = 0.025$ (1600 × 400), $\Delta\mu = 0.1$ and $\Delta\eta = 0.0125$ (400 × 800), and $\Delta\mu = 0.1$ and $\Delta\eta = 0.00625$ (400 × 1600). It can be seen that results from the last four meshes are nearly the same. Small variations are localized and appear only near the end of the separation bubble ($5 < \mu < 6$) from which the unsteady waves are shed, and the mean streamwise velocity changes from negative

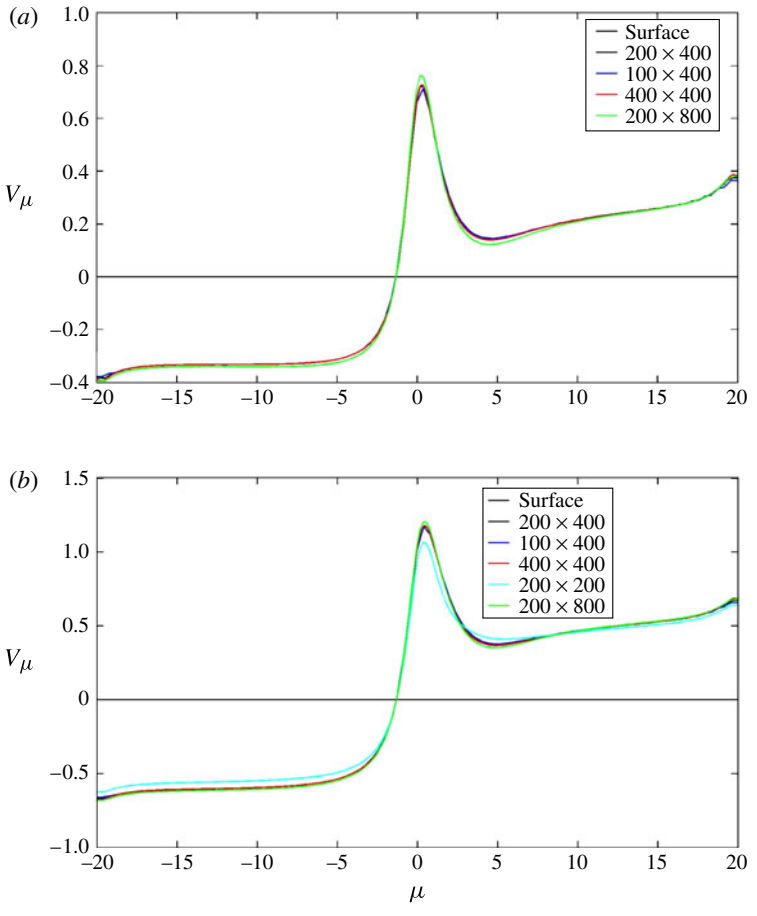

FIGURE 6. (Colour online) Mesh refinement study: $Re_M = 700$; $\tilde{A} = 1.3$; (*a*) $\eta = 1.025$, (*b*) $\eta = 1.05$.

to positive. This may be related to the complicated behaviour of the flow near the reattachment point, i.e. the van Dommelen & Shen (1980) singularity. Also shown in figure 7 is the instantaneous streamwise velocity along grid line $\eta = 2.5$, which is away from the parabola surface and at the edge of the boundary layer. The convergence of this profile with mesh refinement is evident. Moreover, the profiles demonstrate that flow unsteadiness decays with distance from the wall and is bounded to evolving eddies within the boundary layer. This demonstrates that the use of the far-field steady conditions (at $\eta = 11$) is not affected by the natural flow unsteadiness in the boundary layer.

Further, we focus on mesh refinement studies of the power spectrum density (fast Fourier transform, FFT, analysis) of the computed unsteady streamwise velocity V_μ along grid line $\eta = 1.025$ (wall-adjacent grid line). The analysis is based on a data series of 1 million time steps after simulations had stabilized on a periodic flow. Note that obtaining convergence of computed spectra is difficult in comparison to experiments. A moving-average filter on the computed FFT curves has been employed to slightly smooth the spectrum graph. The window of averaging was 15 points. The

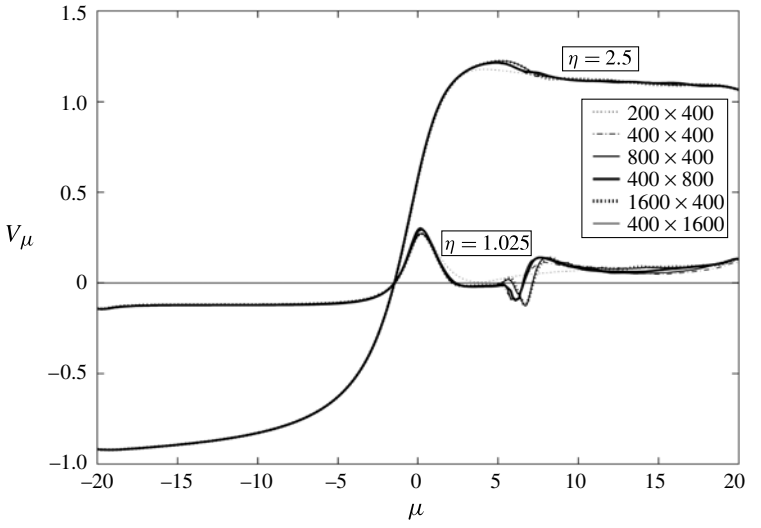

FIGURE 7. Mesh refinement study of time-averaged streamwise velocity along $\eta = 1.025$ and of instantaneous velocity at $\eta = 2.5$ for $Re_M = 700$ and $\tilde{A} = 1.5$.

computed FFT results for two cases where $Re_M = 700$ and $\tilde{A} = 1.5$ and 1.8 at a representative point $\eta = 1.025$, $\mu = 6$ (behind the end of the separation bubble and where the unsteady eddies are shed) are shown in figure 8. The horizontal axis is the non-dimensional frequency f (frequency scaled by $2\pi R_c/U_\infty$). For both cases, the point spectrum dominant frequencies from the finer meshes (400 × 800), (800 × 400) and (1600 × 400) are practically converged with the mesh refinement in both the streamwise and vertical directions. The difference of dominant shedding frequencies that appear at $\tilde{A} = 1.8$ around $f = 0.064$ from these meshes is less than 0.005.

Finally, it should also be noted that, in spite of the small localized differences in the time-averaged velocity profiles and in the dominant frequencies displayed by the FFTs, the global results for the numerical value of the circulation parameter at the onset of stall remain nearly the same from computations using all meshes mentioned above. For example, all meshes show at $Re_M = 700$ that $\tilde{A}_s$ of global stall onset is between 1.8 and 1.9, i.e. $\tilde{A}_s \sim 1.85 \pm 0.05$. In the case of a NACA 0012 wing section this range represents a quarter of a degree accuracy in determining the stall angle of attack, which is below the experimental accuracy of measurement. Also, the dominant frequencies of the unsteady waves before stall onset are resolved within a range of 7 % by the finer meshes. In the case of a NACA 0012 wing section with a chord of 0.2 m at a speed of 10 m s^{-1} and angle of attack of 9° the results for $\tilde{A} = 1.8$ represent a dominant frequency of 31.5 ± 2.5 Hz before the onset of stall, where again the margin of uncertainty is below the experimental accuracy of measurement.

The mesh (400 × 800) provides sufficiently converged results for the unsteady flow cases. This mesh is therefore used in all the flow simulations at $Re_M = 700$ and below, where unsteady waves appear.

We also studied the effect of increasing the domain axial width μ_{max} from 20 to 40 ($\mu_{min} = -\mu_{max}$), maintaining $\Delta\mu = 0.2$ and $\Delta\eta = 0.025$. Results of the velocity V_μ along the grid lines $\eta = 1.025$ (near the wall) and 1.5 (near the boundary-layer edge) for the representative case of $Re_M = 100$ and $\tilde{A} = 1.7$ are shown in figure 9. In

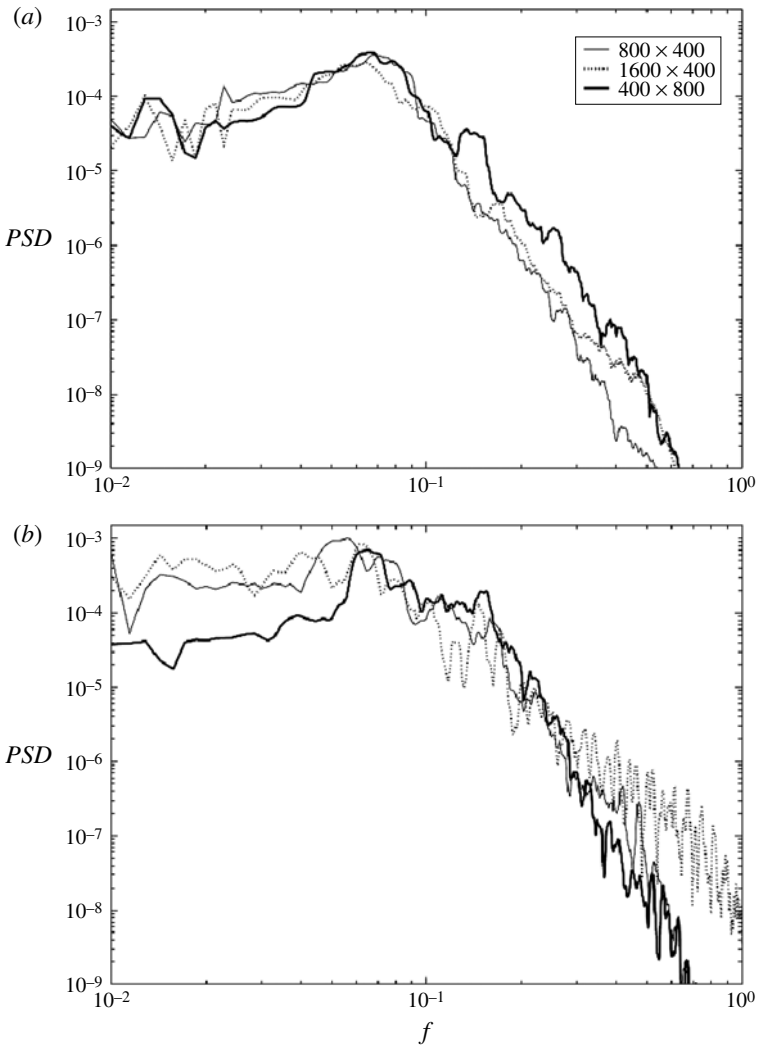

FIGURE 8. Mesh refinement study of FFT results at $\eta = 1.025$ and $\mu = 6$: $Re_M = 700$; (*a*) $\tilde{A} = 1.5$, (*b*) $\tilde{A} = 1.8$.

this case, there is a marginal separation zone and the state is just prior to the value of $\tilde{A}$ for global separation. We can see that the computed results fully agree in the range of $\mu = -15$ to 15 (which is more than 100 radii of curvature from the parabola leading edge). However, beyond this range, the numerical end-effects related to the choice of μ_{max} slightly affect the velocity profile. It is concluded that, for the range of parameters presented here, $\mu_{max} = 20$ is sufficient for accurate resolution of flow details around the nose.

4.2. *Flow simulation results*

In the following, we study viscous flow around the stationary parabola at various Re_M and increasing values of $\tilde{A}$ until global, massive separation (stall) is observed at a certain $\tilde{A} = \tilde{A}_s$. Onset of stall is identified as the state at which the peak streamwise

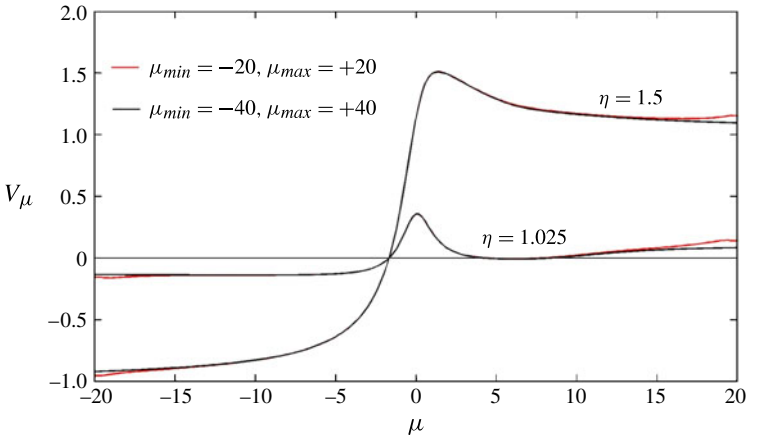

FIGURE 9. (Colour online) Domain size effect: $Re_M = 100$; $\tilde{A} = 1.7$.

velocity V_μ all across the boundary layer ahead of the separation zone either fails to increase or decreases with an increase of circulation parameter (angle of attack), accompanied by a significant eruption of the separated zone from the upper surface. This definition applies to both steady and unsteady flows. In the case of unsteady flows, stall is additionally accompanied by a change of shedding frequency behind the separation zone.

To identify stall, we first plot the wall-adjacent streamwise velocity V_μ distributions near the parabola leading edge. The wall-adjacent streamwise velocity is directly proportional to the wall shear stress coefficient, i.e. when the wall-adjacent streamwise velocity vanishes so does the wall shear stress, indicating separation and reattachment points. Once there is a decrease of peak streamwise velocity along the wall-adjacent grid line, the same happens in the streamwise velocity all across the boundary layer from the wall to the edge of the boundary layer. This event is therefore directly related to loss of peak suction and stall. To demonstrate this event for $Re_M = 100$, we present the wall-adjacent V_μ near the parabola leading edge in figure 10 at various values of $\tilde{A}$. It can be seen that the peak streamwise velocity (suction and therefore lift) increases as $\tilde{A}$ increases from 0 to 1.75 and then suddenly decreases when $\tilde{A}$ increases from 1.75 (thick solid line) to 1.76 (thick dotted line). A similar identification of stall with unsteady flow situations is shown later on for $Re_M = 700$. Note that in the range of Re_M studies in this paper the loss of suction and stall is moderate compared to the abrupt stall that occurs at high Re_M: see figures 2 and 6 in Rusak & Morris (2011) for comparison.

The time-asymptotic (steady) V_μ profiles along equispaced grid lines within the boundary layer, from $\eta = 1$ (the wall) to 1.325 (the boundary-layer edge), are shown in figures 11 and 12 for $Re_M = 100$ and $\tilde{A} = 0.0$ and 1.7, respectively. Along the vertical axis are the values of streamwise velocity and the horizontal axis shows the position along the surface. Note that the far-field speed $V_{\eta\infty} = -1$. Figure 11 shows the $\tilde{A} = 0.0$ case. As expected, the flow field is symmetric between the upper and lower surfaces of the parabola with the stagnation point occurring at the parabola's leading edge. We can also see that the boundary layer is well resolved. With an increase of $\tilde{A}$, the stagnation point (maximum pressure) moves under the nose to the lower surface and a velocity peak (maximum suction point) occurs on the upper surface all across the

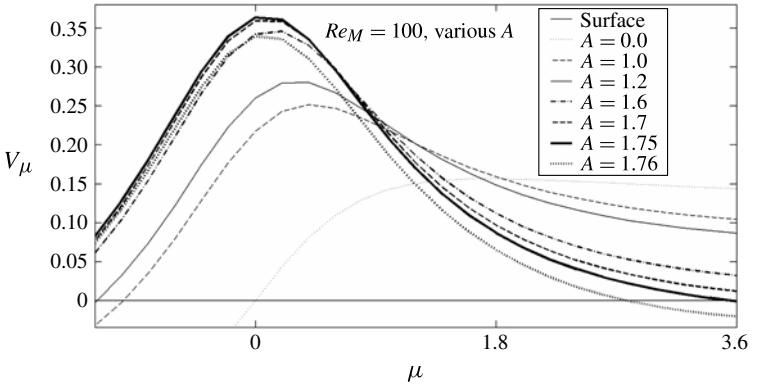

FIGURE 10. A representative demonstration of stall $Re_M = 100$: streamwise velocity near the parabola leading edge along the surface-adjacent grid line at various $\tilde{A}$. Note that the increase of maximum streamwise velocity ceases when $\tilde{A}$ increases from 1.75 to 1.76, indicating loss of peak suction and therefore stall.

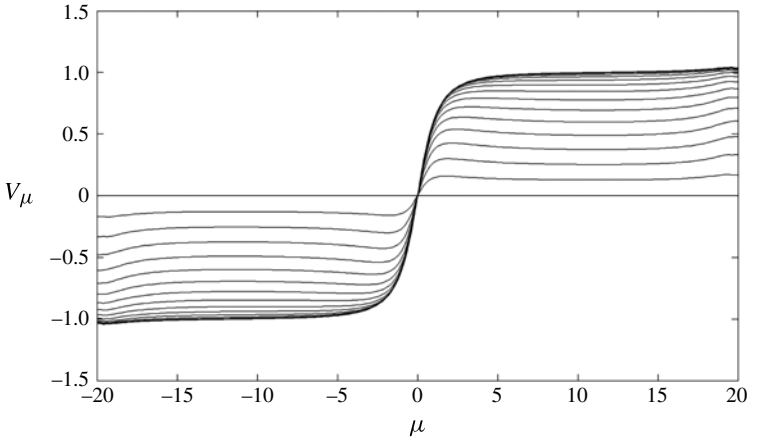

FIGURE 11. For $Re_M = 100$ and $\tilde{A} = 0.0$, V_μ velocity profiles along 13 equispaced grid lines in the boundary layer, from $\eta = 1$ (wall) to 1.325 (boundary-layer edge). Lower surface is μ between -20 to 0; upper surface is μ between 0 to 20. In the computational space streamwise velocities below the lower surface are negative.

boundary layer, just downstream of the leading edge. Following the peak velocity is a velocity dip, or slow-down aft of the suction peak, with a recovery at a distance away from the nose. Figure 12 shows this trend for $\tilde{A} = 1.7$. However, in this case the induced velocity dip by $\tilde{A}$ is sufficiently large to cause a small recirculation zone on the upper surface to appear for the first time. In figure 13 we view the same steady, marginal separation flow field in the physical space around the canonic parabola, where the localized separation zone on the upper surface is clearly evident. This area of negative velocity corresponds to a marginal separation zone, yet the flow is still globally attached.

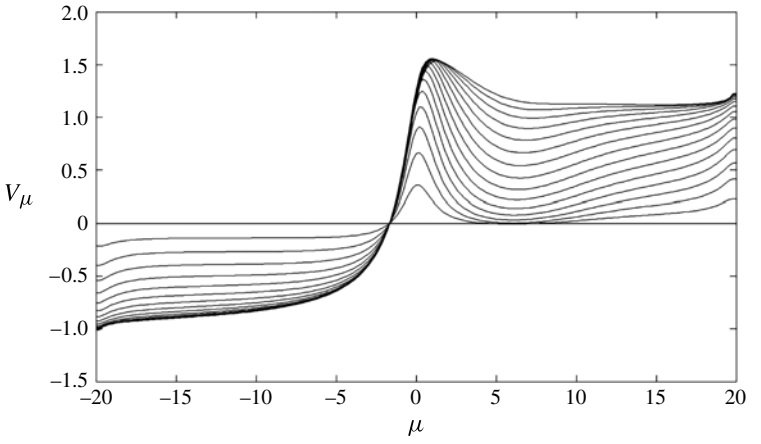

FIGURE 12. V_μ velocity profiles in the boundary layer for $Re_M = 100$ and $\tilde{A} = 1.70$ along 13 equispaced grid lines in the boundary layer, from $\eta = 1$ (wall) to 1.325 (boundary-layer edge).

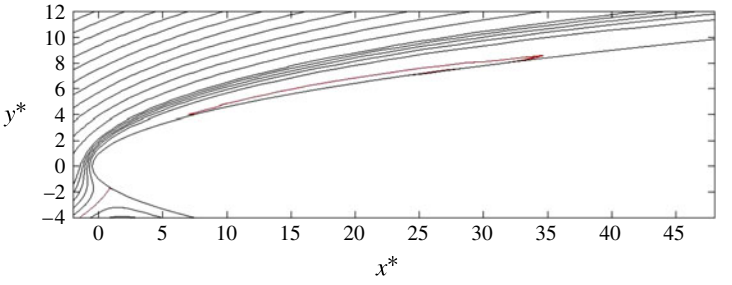

FIGURE 13. (Colour online) Streamline contours for $Re_M = 100$ and $\tilde{A} = 1.70$: steady marginal separation state. The separation zone contour on the upper surface is evident.

The computed, time-asymptotic streamline contours around the parabolic nose, with further increases of $\tilde{A}$ at $Re_M = 100$, are shown in figures 14–16. In figure 14, $\tilde{A} = 1.73$ and the marginal separation zone increases in size with respect to that at $\tilde{A} = 1.70$ (shown in figure 13). In figure 15, $\tilde{A} = 1.75$ and there is a further increase in size of the separation zone. However, figure 10 shows that the maximum streamwise velocity (and suction) continues to increase as $\tilde{A}$ increases from 1.7 to 1.75. In figure 16, $\tilde{A}$ is increased from 1.75 to 1.77 and a global separation zone dominates the flow. It is accompanied by a decrease of maximum streamwise velocity and suction: see figure 10. This is leading-edge stall. The figures demonstrate the transition from marginal separation to global separation (stall) as $\tilde{A}$ is increased from 1.75 to 1.77, and $\tilde{A}_s = 1.76$ for $Re_M = 100$.

With this information we can compute the angle for the first appearance of separation and the stall angle for the NACA 0012 wing section at $Re = 6300$ (which corresponds to $Re_M = 100$) according to both MST and present calculations. From the present simulations the critical points correspond to an angle of attack for first separation of 8.7° and a stall angle of 9.0°. From MST (Sychev *et al.* 1998, p. 172), predictions of the respective angles are 7.9 and 8.1°. The two approaches predict

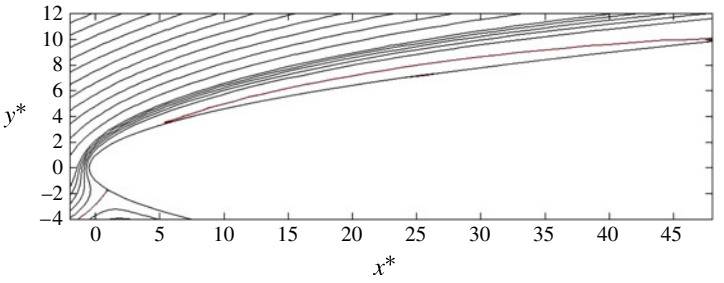

FIGURE 14. (Colour online) Streamline contours for $Re_M = 100$ and $\tilde{A} = 1.73$. The separation zone contour on the upper surface is evident.

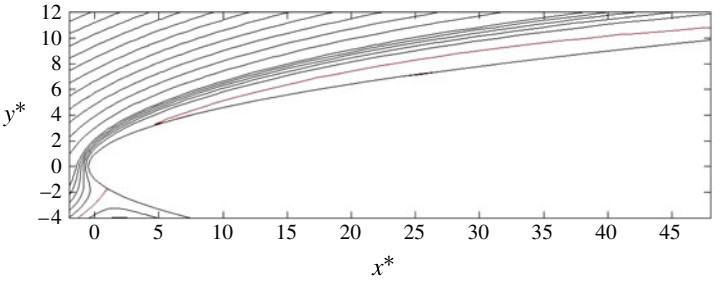

FIGURE 15. (Colour online) Streamline contours for $Re_M = 100$ and $\tilde{A} = 1.75$. The separation zone contour on the upper surface is evident.

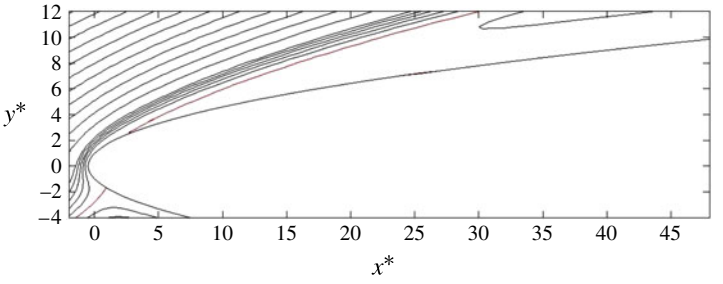

FIGURE 16. (Colour online) Streamline contours for $Re_M = 100$ and $\tilde{A} = 1.77$: steady stall state. The separation zone contour on the upper surface is evident.

similar stall angles. Differences between the results may correspond to errors in both formulations, such as neglect of higher-order terms in MST and discretization errors in the present simulations.

At this point we seek to demonstrate the possible existence of a stall hysteresis loop by reducing $\tilde{A}$ in small steps. When $\tilde{A}$ is reduced from 1.77 to 1.76 the same globally separated flow solution is reached as when increasing $\tilde{A}$ from 1.75 to 1.76, demonstrating that there may exist only one solution of the flow for $\tilde{A} \geqslant 1.76$. However, when $\tilde{A}$ is further reduced to 1.75 and to 1.73 it is found that the flow remains globally separated: see the time-asymptotic streamline contours in figures 17

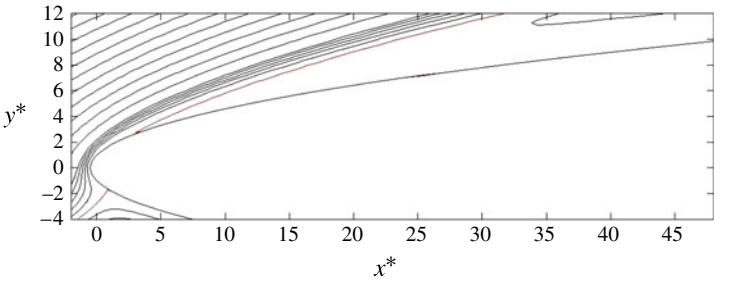

FIGURE 17. (Colour online) Streamline contours over velocity magnitude field for $Re_M = 100$ and $\tilde{A} = 1.75$ descending. The separation zone contour on the upper surface is evident.

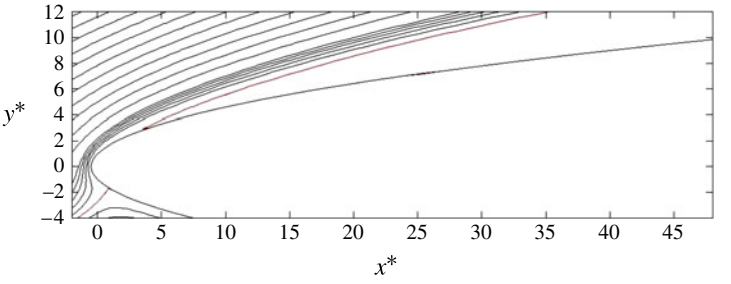

FIGURE 18. (Colour online) Streamline contours over velocity magnitude field for $Re_M = 100$ and $\tilde{A} = 1.73$ descending. The separation zone contour on the upper surface is evident.

and 18, respectively. Note that these states are different from the marginal separation states found when $\tilde{A}$ was increased from 1.7 to 1.73 and to 1.75 (compare figures 17 and 18 with figures 14 and 15). This demonstrates the coexistence of time-asymptotic states at these values of $\tilde{A}$. The flow does return to a small separation zone only when $\tilde{A}$ is decreased from 1.73 to 1.72. With further decrease of $\tilde{A}$ below 1.72, the simulations provide the same result as found for the ascending circulation parameter cases.

This demonstrates the existence of a stall-hysteresis loop with a maximal range between $\tilde{A} = 1.72$ and 1.76 for $Re_M = 100$. Two different steady flow states exist in this range, one describing a marginally separated state and the other a globally separated stall state. When this information is used for a NACA 0012 wing section, it indicates a range of stall-hysteresis of 0.2° at $Re = 6300$ – a small value, generally undetectable by experimental methods.

The stall hysteresis loop at $Re_M = 100$ is also demonstrated in figure 19. Here we plot the minimum of streamwise velocity V_μ along the wall-adjacent grid line above the upper surface ($\eta = 1.025$) versus the change in circulation parameter $\tilde{A}$. The arrows along the line show the direction of hysteresis loop. The minimum of V_μ decreases to small negative values with the increase of $\tilde{A}$ toward $\tilde{A}_s$, it remains nearly constant (~ -0.03) for all stalled states, and then it increases as $\tilde{A}$ is reduced below the range of hysteresis and flow returns to a globally attached state.

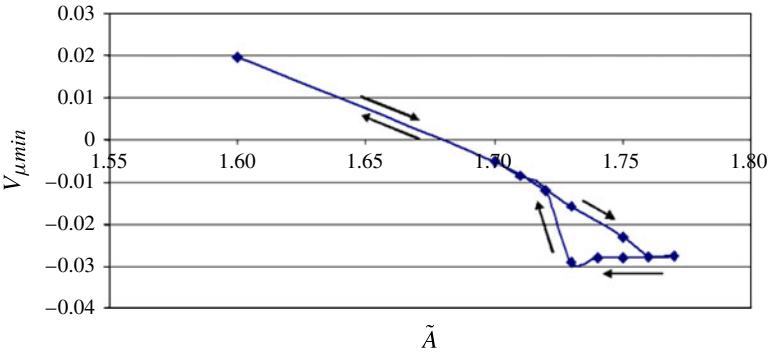

FIGURE 19. (Colour online) Minimum of V_μ along $\eta = 1.025$ on the upper surface as a function of the circulation parameter. The hysteresis loop for $Re_M = 100$ at $\tilde{A}$ in the range 1.72 to 1.76 is demonstrated.

Similar to the $Re_M = 100$ case, computed results show attached flow states for $Re_M = 200$ when $\tilde{A} < 1.56$ (see, for example, the streamline contours at $\tilde{A} = 1.5$ in figure 20*a*) and for $Re_M = 300$ when $\tilde{A} < 1.48$ (see figure 21*a* exhibiting a marginally separated zone at $\tilde{A} = 1.5$). More detailed computations show that the first appearance of a marginal separation zone for $Re_M = 200$ is at $\tilde{A} = 1.56$, and when $\tilde{A}$ is further increased to 1.62 the flow exhibits a global separation and stall (see the streamline contours of the post-stall state at $\tilde{A} = 1.65$ in figure 20*b*). Global separation for $Re_M = 300$ is first found at $\tilde{A} = 1.55$ (see the streamline contours of the post-stall state at $\tilde{A} = 1.6$ in figure 21*b*). We find that $\tilde{A}_s = 1.62$ for $Re_M = 200$ and $\tilde{A}_s = 1.55$ for $Re_M = 300$. The computations for Re_M up to 300 demonstrate that values of $\tilde{A}$ for the first appearance of separation and of global stall decrease with the increase of Re_M (compare figures 20*a*, 21*a*, both at $\tilde{A} = 1.5$). This is again in agreement with predictions of MST as discussed for the case of $Re_M = 100$. Moreover, the computations show that at $Re_M = 100$ the separation and global separation are laminar and steady. Note that unsteady vorticity waves that propagate downstream appear at the post-stall states inside the globally separated zones and the shedding point moves upstream when Re_M is increased from 100 to 300. At $Re_M = 300$ the unsteady eddies appear with the onset of global stall.

When Re_M is increased above 300 the flow exhibits unsteadiness in the globally attached flow (pre-stall) states for all values of $\tilde{A}$ that are above those that correspond to the MST stall prediction. For example, for $Re_M = 500$ the flow is fully attached and steady up to $\tilde{A} = 1.4$ (which is just below the MST stall prediction): see figure 22(*a*). An instantaneous view of streamline contours in figure 22(*b*) shows an unsteady globally attached state at $\tilde{A} = 1.5$ with localized separations generated by small shedding vortical eddies. In this case, the streamwise velocity above and all along the parabola upper surface remains positive in the mean. As $\tilde{A}$ is increased further, the unsteady waves grow in size with the increase in width of the boundary layer. Ultimately, a globally unsteady separated flow is found at $\tilde{A} = 1.68$, where the streamwise velocity near the parabola upper surface becomes negative, even in the mean, and the maximum streamwise velocity along the grid line adjacent to the wall does not grow with $\tilde{A}$. We find that $\tilde{A}_s = 1.68$ for $Re_M = 500$. These computations

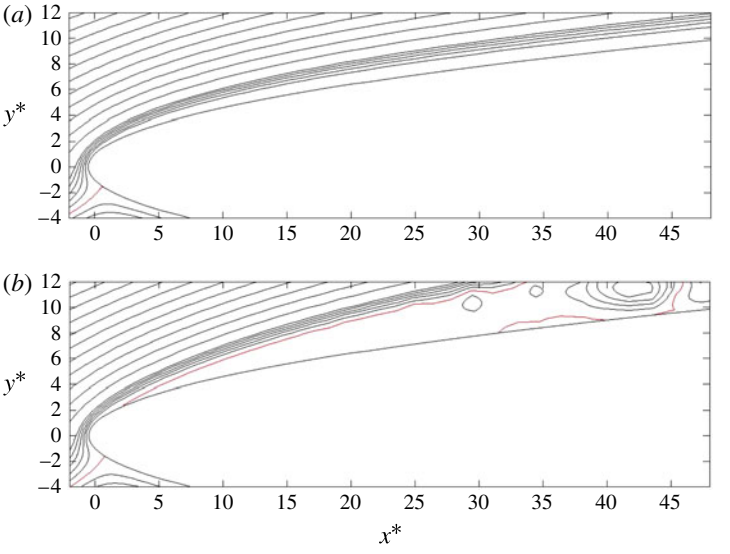

FIGURE 20. (Colour online) (*a*) Streamline contours for $Re_M = 200$ and $\tilde{A} = 1.5$: attached steady state. (*b*) Streamline contours for $Re_M = 200$ and $\tilde{A} = 1.65$: stalled unsteady state.

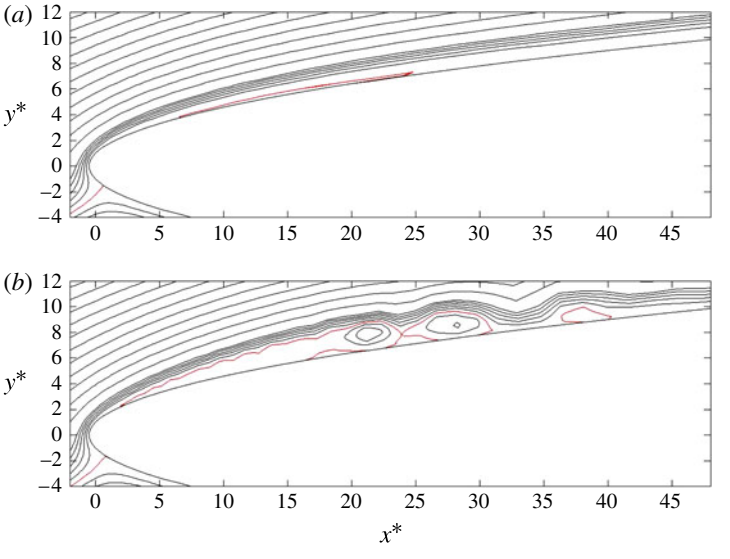

FIGURE 21. (Colour online) (*a*) Streamline contours for $Re_M = 300$ and $\tilde{A} = 1.5$: marginally separated steady state. (*b*) Streamline contours for $Re_M = 300$ and $\tilde{A} = 1.6$: unsteady stall state. Closed contours indicate the recirculation zones and the shedding of localized vortical eddies.

demonstrate the appearance of unsteadiness in the pre-stall states and an increase of both values of $\tilde{A}$ for the first appearance of separation and for global stall when Re_M is above 300. We define $Re_M = 300$ as the *limit Reynolds number* for laminar and steady global stall states over the parabola (aerofoil nose).

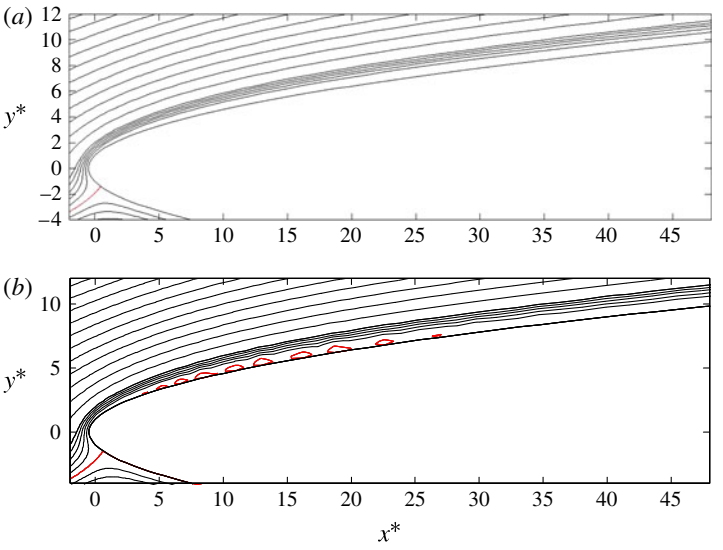

FIGURE 22. (Colour online) (*a*) Streamline contours for $Re_M = 500$ and $\tilde{A} = 1.4$: attached steady state. (*b*) Streamline contours for $Re_M = 500$ and $\tilde{A} = 1.5$: unsteady globally attached state. Closed contours indicate the shedding of localized vortical eddies along the upper surface.

The flow states at $Re_M = 700$, which is sufficiently above the limit value $Re_M = 300$, are studied in detail. The flow is fully attached up to $\tilde{A} = 1.4$ (which is slightly above the MST stall prediction for this case): see figure 23(*a*). When $\tilde{A}$ is increased above 1.4 (see, for example, figure 23*b* at $\tilde{A} = 1.5$, figure 23*c* at $\tilde{A} = 1.7$, and figure 23*d* at $\tilde{A} = 1.8$), unsteady globally attached states are found with a local, steady clockwise recirculation zone near the leading edge, followed by a secondary anticlockwise recirculation zone and a tertiary eddy that breaks away and is the source of coherent eddies that convect downstream. Similar states were also observed in Bhaskaran & Rothmayer (1998). The steady separation bubble decreases in axial length with increase of $\tilde{A}$. However, the streamwise velocity at these states above and along the upper surface remains only slightly negative in the mean. The maximum streamwise velocity found all across the boundary layer ahead of the separation zone continues to grow with $\tilde{A}$, indicating a continued build-up of suction (lift) near the leading edge: see figure 24. However, when $\tilde{A}$ is further increased to 1.9 (figure 23*e*), a stalled state develops. It is characterized by shorter and wider clockwise and anticlockwise recirculation zones above the parabola upper surface along with no increase of the maximum streamwise velocity (suction) ahead of the separation zone with $\tilde{A}$ (with respect to results for $\tilde{A} = 1.8$: see again figure 24). The tertiary and convective eddies also increase in width. This indicates a stalled state. Detailed computations show that $\tilde{A}_s = 1.88$ for $Re_M = 700$. The computations demonstrate the further increase of the value of $\tilde{A}_s$ for appearance of global stall with increase of Re_M above 300. The unsteady post-stall state at $\tilde{A} = 2$ shows the further increase in size of the separation zone and of the vortical eddies that convect downstream: see figure 23(*f*).

As for the $Re_M = 100$ case, we seek to demonstrate the possible existence of a stall hysteresis loop at $Re_M = 700$ by reducing $\tilde{A}$ in small steps. When $\tilde{A}$ is reduced from 2

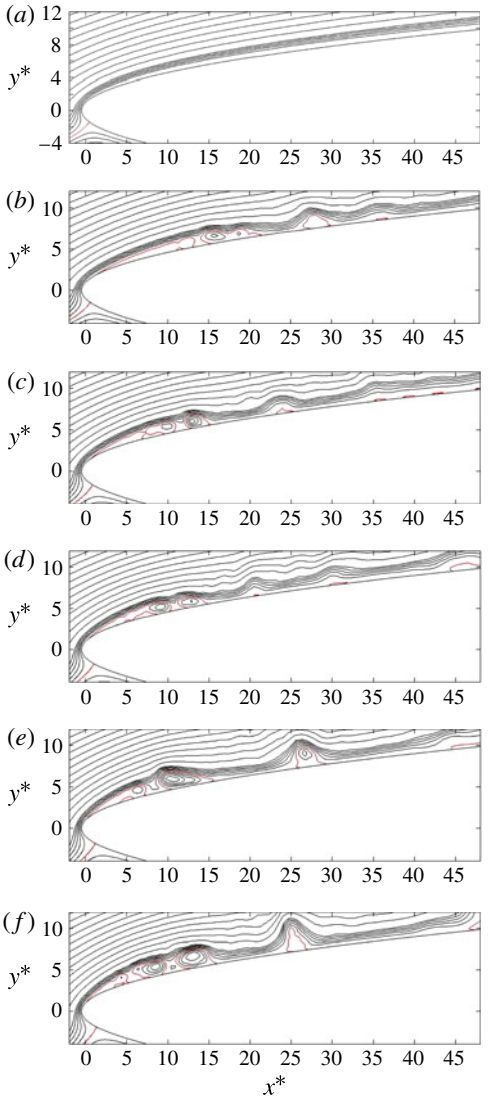

FIGURE 23. (Colour online) Streamline contours for $Re_M = 700$ at: (*a*) $\tilde{A} = 1.4$: attached steady state. (*b*) $\tilde{A} = 1.5$: unsteady globally attached flow (instantaneous view). (*c*) $\tilde{A} = 1.7$: unsteady globally attached flow (instantaneous view). (*d*) $\tilde{A} = 1.8$: unsteady globally attached state (instantaneous view). (*e*) $\tilde{A} = 1.9$: unsteady post-stall state (instantaneous view). (*f*) $\tilde{A} = 2$: unsteady post-stall state (instantaneous view). Closed contours in all frames indicate the recirculation zones and the shedding of vortical eddies.

to 1.9 (see figure 25*a*) the same globally separated, unsteady flow solution is reached as when increasing $\tilde{A}$ from 1.8 to 1.9 (compare with figure 23*c*). This suggests that the flow dynamics has only a global stall time-asymptotic state for $\tilde{A} \geqslant \tilde{A}_s = 1.88$ (no globally attached time-asymptotic state is found in this range of $\tilde{A}$). However, when $\tilde{A}$ is further reduced to 1.8 it is found that the flow remains globally separated: see an instantaneous state of the flow in figure 25(*b*). This demonstrates the coexistence

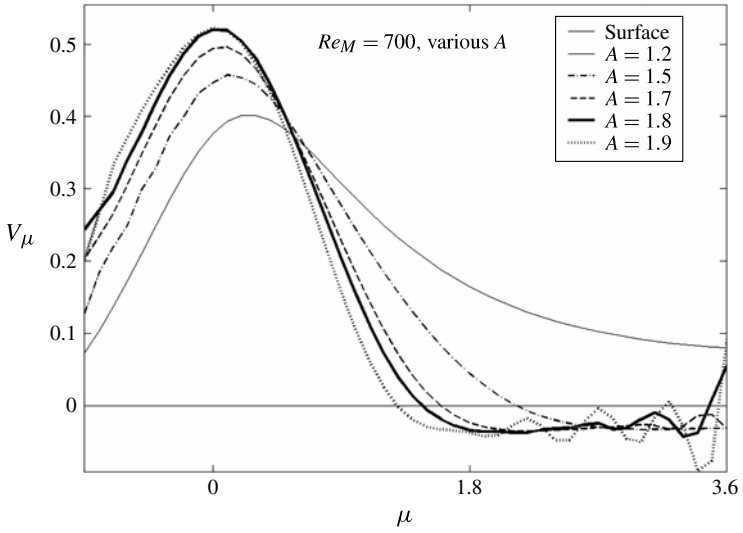

FIGURE 24. Streamwise velocity near the parabola leading edge along the surface-adjacent grid line at various $\tilde{A}$. Note that the increase of maximum streamwise velocity ceases when $\tilde{A}$ increases from 1.8 to 1.9, indicating loss of suction and therefore stall.

of two time-asymptotic states at this value of $\tilde{A}$. The flow returns to an unsteady globally attached state only when $\tilde{A}$ is decreased to 1.75 and below. This demonstrates the existence of a stall hysteresis loop with a maximal range between $\tilde{A} = 1.75$ and 1.88 for $Re_M = 700$. Two different flow states exist in this range, one describing an unsteady globally attached state and the other a globally stalled state. When this information is used for a NACA 0012 aerofoil, it indicates a range of stall hysteresis of 0.8° at $Re = 44\,000$ – a small yet finite range, that can be detected by experimental methods.

Using the various snapshots of figure 23, we plot the separated zone thickness at the end of the static leading-edge bubble as a function of $\tilde{A}$: see figure 26. This is identified by the height of the $\psi = 5$ contour line above the parabola upper surface. The figure again demonstrates the onset of stall when $\tilde{A} > 1.88$ and the hysteresis loop at $Re_M = 700$. There is a clear increase in the zone thickness as $\tilde{A}$ is increased from 1.8 to 1.9 and to 2, indicating the onset of stall. The stall state persists as $\tilde{A}$ is decreased from 2 to 1.9 and to 1.8. The flow resumes an attached unsteady flow state at $\tilde{A} = 1.75$.

We now present results of a power spectral (FFT) analysis of the computed unsteady streamwise velocity V_μ along a wall-adjacent grid line around the parabola surface for $Re_M = 700$ when $\tilde{A} > 1.4$. We focus on a point $\mu = 6$, $\eta = 1.025$ ($x^* = 17.49$, $y^* = 5.9$) where the coherent convective waves are observed for all $\tilde{A} > 1.4$, and identify the dominant non-dimensional frequency $f_{dominant}$ (frequency scaled by $2\pi R_c/U_\infty$) with the maximum energy for each $\tilde{A}$. The results are summarized in figure 27. At the attached flow states $\tilde{A} < 1.4$ the flow is steady and $f = 0$ for all points on the parabola. At the unsteady, pre-stall state of $\tilde{A} = 1.4$ there is a sudden increase of $f_{dominant}$ to 0.062. The dominant frequency stays around 0.064 for the range $1.5 \leqslant \tilde{A} \leqslant 1.8$. As $\tilde{A}$ is increased further, $f_{dominant}$ also increases to 0.09 at $\tilde{A} = 1.9$ and $\tilde{A} = 2$. The spectral analysis

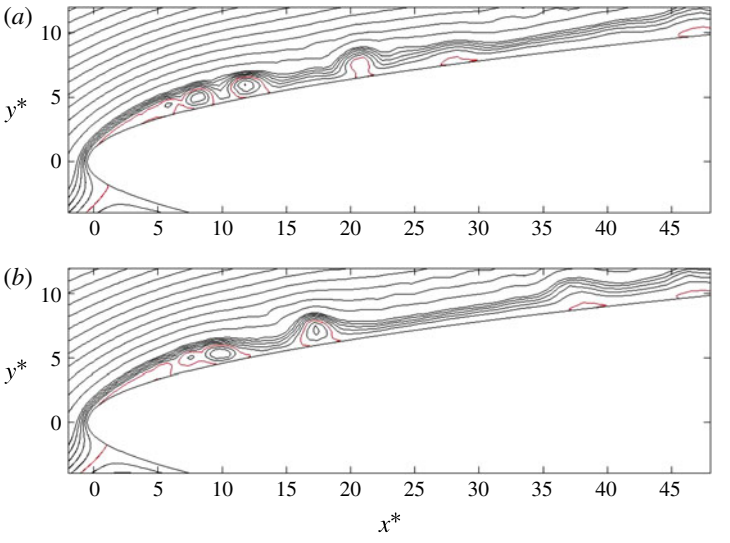

FIGURE 25. (Colour online) A snapshot of streamline contours for $Re_M = 700$ at: (*a*) $\tilde{A} = 1.9$ descending: unsteady stall state. (*b*) $\tilde{A} = 1.8$ descending: unsteady stall state. Closed contours in the frames indicate the recirculation zones and the shedding of vortical eddies.

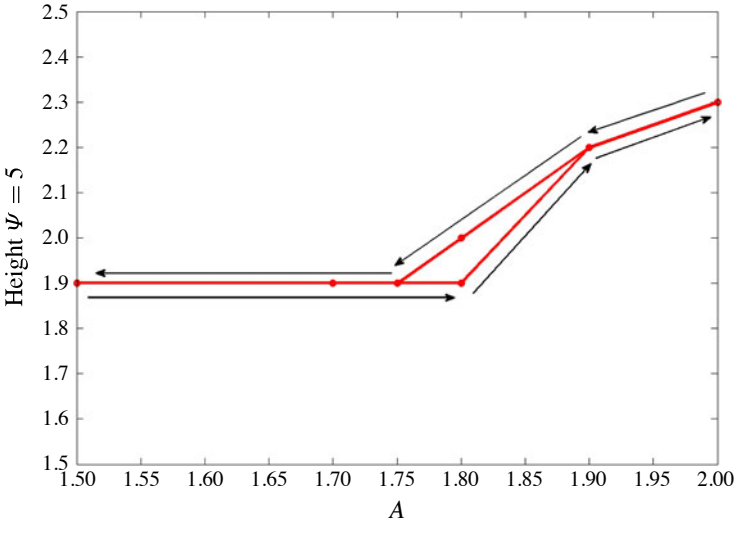

FIGURE 26. (Colour online) Demonstrating the hysteresis stall loop at $Re_M = 700$ from the separation zone thickness at the end of the static leading-edge bubble as a function of $\tilde{A}$ in the range 1.5 to 2.

shows an increase of dominant frequency as the flow turns from pre- to post-stall states (as $\tilde{A}$ is increased). As $\tilde{A}$ is decreased back along the stall hysteresis loop, the frequency stays nearly constant ($\sim$0.09). Then it decreases and as the flow reattaches, a pre-stall dominant frequency is recovered. This change of dominant frequency can be used as an additional indicator for the onset of leading-edge stall and an observability

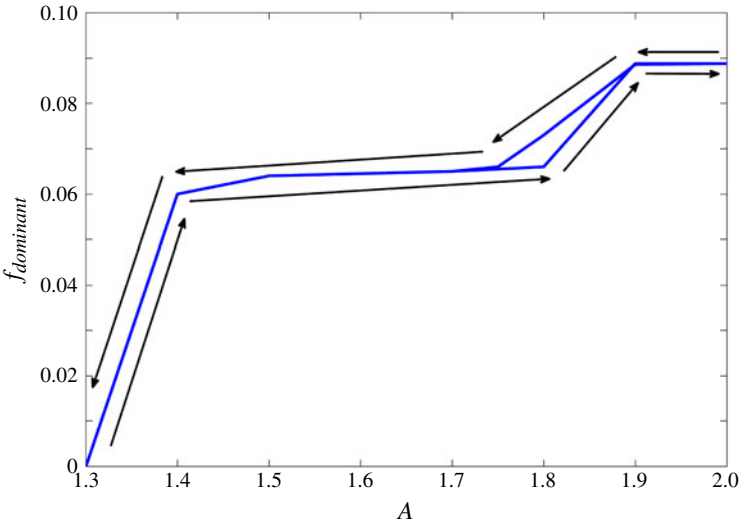

FIGURE 27. (Colour online) Variation of the dominant frequency at the point $\mu = 6$, $\eta = 1.025$ with $\tilde{A}$ for $Re_M = 700$.

parameter for control methodologies to delay stall: see, for example, the experimental study by Pinier *et al.* (2007).

The convective waves observed in figures 23 and 25 are characterized by dominant low-frequency convection of energy along the boundary layer downstream away from the near-separation region. This helps the boundary layer to overcome the pressure gradient influence and maintain a globally attached state. Moreover, we find that as the external adverse pressure gradient becomes stronger with the increase of circulation parameter in the range $\tilde{A} < \tilde{A}_s$, the convective waves' frequency slightly increases. This allows the convection of energy downstream to further maintain a globally attached state. However, once $\tilde{A} > \tilde{A}_s$ and a global stall appears, the greater adverse pressure gradient dominates the flow and even the unsteady convective waves are not able to remove enough energy to maintain the boundary layer in an attached state. This shows that when $Re_M > 300$ the convective unsteady coherent structures (which appear at values of $\tilde{A}$ slightly above MST prediction) become an integral part of the critical balance between the viscous stresses in the boundary layer and the external adverse pressure gradient. The balance between these three effects determines whether the boundary layer is globally attached or stalled.

Additional simulations with further refined meshes at $Re_M = 1000$ and 2100 were conducted, and exhibited similar behaviour. We find that at $Re_M = 1000$ flow unsteadiness appears when $\tilde{A} > 1.3$ and global stall onset occurs at $\tilde{A}_s = 2.05$. At $Re_M = 2100$ flow unsteadiness appears when $\tilde{A} > 1.2$ and global stall onset occurs at $\tilde{A}_s = 2.4$.

The main results of the present simulations for Re_M in the range 100 to 2100 are summarized in figure 28. The computed universal lines of $\tilde{A}$ versus Re_M for the onset of unsteadiness and global stall are shown. The line for the onset of unsteadiness (dotted line) starts from $Re_M = 300$, decreases monotonically with Re_M, and is just above the predicted stall line according to MST (Ruban 1982; Stewartson *et al.* 1982).

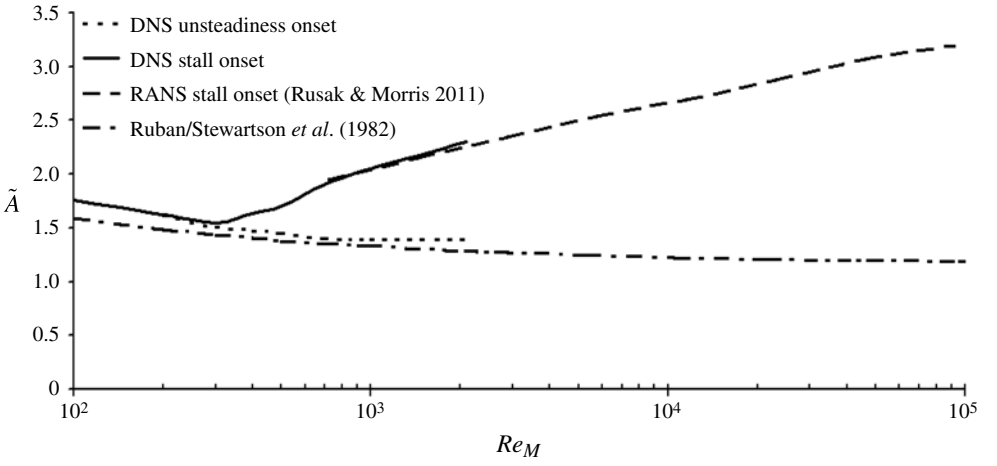

FIGURE 28. Summary of computed results: dotted line, unsteadiness onset according to DNS computations; solid line, global stall onset according to DNS computations; dashed line, global stall onset according to RANS computations; dot-dashed line, stall onset according to MST.

The line of global stall onset decreases up to the limit Reynolds number $Re_M = 300$ and then reverses trend and increases with Re_M. Moreover, in the range of $Re_M > 700$ this line overlaps with the global stall onset line computed in Rusak & Morris (2011) using a Reynolds-averaged Navier–Stokes (RANS) solver and employing the same canonic model problem for high Re_M flows (in the range between 700 and 100 000, where accurate DNS simulations require a great deal of computational power).

The universal results from figure 28 are now used to calculate the properties of the NACA 0012 wing section at a wide range of Re (based on the chord) from the relatively low value of 6300 (which corresponds to $Re_M = 100$) up to the moderately high value of $Re = 132\,500$ (which corresponds to $Re_M = 2100$), and are added to figure 1: see the compiled results in figure 29. Note that according to available data (e.g. McCormick 1995; Anderson 2007), the flow over a smooth wing section in this range of Re does not experience transition to turbulence in the nose region, yet unsteady convective waves may appear. The numerical simulations calculated values of angle of attack at onset of unsteadiness and onset of global stall are given by the dotted and solid lines, respectively. Results from the Rusak & Morris (2011) RANS canonic parabola calculations for Re between 40 000 and 9 million are given by the dashed line. Also shown are the Rusak & Morris (2011) results of stall onset using RANS computations for a NACA 0012 wing section at high Re flows in the range of 40 000 to 9 million (dashed line with open squares). The MST predictions for separation onset and stall onset are presented by the shaded solid and dot-dashed lines, respectively. Experimental data for stall onset from the classical studies of Abbott & von Doenhoff (1958) (solid line with diamonds) and Jacobs & Sherman (1937) (solid line with solid squares) and from the recent study of Yen & Huang (2009) (solid line with triangles) are presented. The present simulation results exhibit agreement of the unsteadiness onset with the MST stall prediction (within half a degree) and of the global stall onset with the experimental data and the two RANS computations (within 1.5°). We find that MST prediction may be related to the present simulations' prediction of unsteadiness onset. The simulations' global stall prediction

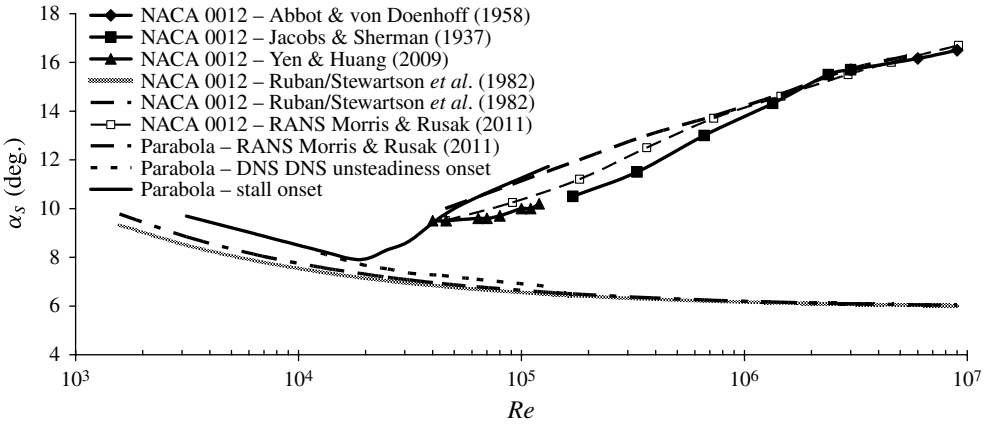

FIGURE 29. Summary of major angles of attack for the NACA 0012 wing section as a function of chord Reynolds number Re: dotted line, unsteadiness onset according to the present simulations; black solid line, global stall onset according to present numerical simulations; dashed line, global stall onset according to Rusak & Morris (2011) RANS computations; shaded solid line, separation onset according to MST; dot-dashed line, stall onset according to MST. Experimental data for stall onset: solid line with diamonds, Abbott & von Doenhoff (1958); solid line with solid squares, Jacobs & Sherman (1937); solid line with triangles, Yen & Huang (2009). The solid line with open squares shows the results from Rusak & Morris (2011) of stall onset using RANS computations for a NACA0012 wing section.

may provide an upper limit for the onset of stall on the aerofoil. This is due to the difference in geometry between a semi-infinite parabola and the aerofoil at some distance away from the leading edge. The parabola can maintain a globally attached flow state at slightly higher angles of attack due to the more favourable pressure gradient that results from its ever-expanding geometry while, in the case of an aerofoil, the geometry narrows beyond the nose region, adding to the adverse pressure gradient and causing a slightly earlier stall.

5. Conclusions

The inception of leading-edge stall on two-dimensional, smooth, thin aerofoils at low to moderately high Reynolds number flows in the range $O(10^3)$ to $O(10^5)$ can be investigated by a reduced-order, multiscale model problem. The model (simplified) problem consists of a uniform incompressible viscous flow past a semi-infinite parabola with a far-field circulation governed by a parameter $\tilde{A}$ that is related to the aerofoil's angle of attack, nose radius of curvature, thickness ratio, and camber. The parameter $\tilde{A}$ determines the pressure gradient along the parabola. Numerical simulations of the unsteady flow are conducted at various Re_M and $\tilde{A}$. The universal values of $\tilde{A}$ for the onset of flow unsteadiness in the form of vortical eddies and of $\tilde{A}_s$ for the onset of a global nose-separation zone are determined as a function of Re_M: see figure 28. Computed results show agreement with marginal separation theory at low Re_M and with available experimental data and RANS computations at higher Re_M: see the example in figure 29.

The present study reveals the fundamental nature of leading-edge stall on a stationary aerofoil. It is found that there exists a limit Re_M ($\sim$300). When Re_M is

below this limit, the flow is laminar and steady, even at post-stall states, and is dominated by the increasing effect of the adverse pressure gradient which eventually overcomes the viscous stresses ability to keep the boundary layer attached to the aerofoil. The present prediction of onset of stall in this flow regime agrees with MST results (Ruban 1982; Stewartson *et al.* 1982): $\tilde{A}_s$ decreases with Re_M. However, when Re_M increases above the limit value of 300 and $\tilde{A}$ is increased beyond the MST prediction for stall, coherent flow unsteadiness appears inside the boundary layer in the form of convective eddies that are shed from the marginal separation zone and, as a result, $\tilde{A}_s$ increases with Re_M. These waves grow in size with either $\tilde{A}$ or Re_M. These unsteady convective structures relax the effect of the adverse pressure gradient on the viscous boundary layer to delay the onset of stall in the mean flow to higher values of $\tilde{A}_s$ compared to MST, in agreement with experimental data.

Beyond these conclusions, this stall mechanism suggests that when additional means to promote shedding are added, additional energy can be convected downstream along the boundary layer, away from the near-separation zone to help delay stall, beyond the natural case, to even higher values of $\tilde{A}$. We are currently conducting studies of flow reattachment and delay of stall by modelling oscillating jet actuators located in front of the separation point and operating at the dominant frequencies shown in figure 27.

Acknowledgements

This research was supported in part by the National Science Foundation's Graduate Research Fellowship Program under award DGE-0237084 for W.J.M.II. The research was also partially supported by the National Science Foundation under award ECS-0523957 for Z.R.

Appendix

A.1. *Outer expansion*

In the outer region, we use the reference parameters c, U_∞, and p_∞ to scale the axial and vertical distances, velocity components, and pressure, respectively. Specifically, $\bar{x} = x/c, \bar{y} = y/c$. The dimensionless equations governing an unsteady, incompressible flow of a Newtonian fluid are (Batchelor 1967)

$$\nabla \cdot \boldsymbol{V} = 0, \tag{A 1}$$

$$\frac{\partial \boldsymbol{V}}{\partial t} + \boldsymbol{V} \cdot \nabla \boldsymbol{V} = -\nabla p + \frac{1}{Re}\nabla^2 \boldsymbol{V}. \tag{A 2}$$

Here $\boldsymbol{V}$ is the dimensionless velocity vector and p is the dimensionless pressure. The flow is governed by the no-slip and no-penetration conditions along the aerofoil surface.

Typically $Re \gg 1$, and the effect of viscosity is localized to the very thin boundary layers and plays only a secondary (or even smaller) role in determining the pressure distribution along the aerofoil. We also assume that the boundary-layer thickness is much smaller than the aerofoil thickness, so that $Re \gg 1/\delta^2$. Then, except for the boundary layers near the aerofoil surface, the flow in the outer region is dominated by the steady and inviscid flow equations with only the no-penetration boundary condition along the aerofoil surface,

$$\nabla \cdot \boldsymbol{V} = 0, \tag{A 3}$$

$$\boldsymbol{V} \cdot \nabla \boldsymbol{V} = -\nabla p. \tag{A 4}$$

The velocity and pressure distributions along the aerofoil surfaces from this inviscid solution are also the velocity and pressure distributions at the edge of the boundary layers.

Since typically the aerofoil's thickness ratio is small ($0 < \delta \ll 1$), it can be shown (see Rusak 1994) that the solution of (A 3) and (A 4) in the outer region (around most of the aerofoil except for the nose region) is dominated by the classical linear aerofoil theory. Then the non-dimensional velocity potential $\bar{\Phi}$, where $\boldsymbol{V} = \boldsymbol{\nabla}\bar{\Phi}$, scaled with $U_\infty c$, is described near the leading edge by the asymptotic expansion

$$\frac{\Phi}{U_\infty c} = \bar{\Phi} \approx \bar{x} + \delta\left(2h\sqrt{\bar{r}}\sin\frac{\theta}{2} + 2Aw_0\sqrt{\bar{r}}\cos\frac{\theta}{2}\right) + O(\bar{r}\log\bar{r}, \bar{r}). \tag{A 5}$$

Here, $\bar{r} = \sqrt{\bar{x}^2 + \bar{y}^2} \to 0$ and $\theta = \arctan(\bar{y}/\bar{x})$. Also,

$$w_0 = 1 - \frac{1}{\pi A}\int_0^\pi \frac{\mathrm{d}C_a}{\mathrm{d}\bar{x}}(\vartheta)\,\mathrm{d}\vartheta, \quad \text{where } \bar{x} = (1 - \cos\vartheta)/2. \tag{A 6}$$

This shows that there is a mis-ordering in the magnitude of the disturbances to a uniform flow for every θ when $\bar{r}$ becomes smaller than R_c. Therefore, a rescaling in the radial direction is needed around the leading edge of the aerofoil.

A.2. *Inner expansion*

In the inner region around the aerofoil's nose ($0 \leqslant x/c < R_c/c$), scaled coordinates and flow parameters are used to correctly describe the local nonlinear behaviour of the flow, which includes the extreme velocity changes due to the near-stagnation and suction areas around the nose. There, we use the nose radius of curvature $R_c = 2\delta^2 h^2 c$ to scale the axial and vertical coordinates $x^* = x/R_c$ and $y^* = y/R_c$ and time is scaled so that $t^* = t\,U_\infty/R_c$. The problem in the nose region becomes, to leading order, the flow of an incompressible, viscous stream described by the dimensionless unsteady Navier–Stokes equations (Rusak 1994):

$$\boldsymbol{\nabla}^* \cdot \boldsymbol{V}^* = 0, \tag{A 7}$$

$$\frac{\partial \boldsymbol{V}^*}{\partial t^*} + \boldsymbol{V}^* \cdot \boldsymbol{\nabla}^* \boldsymbol{V}^* = -\boldsymbol{\nabla}^* p^* + \frac{1}{Re_M}\boldsymbol{\nabla}^{*2}\boldsymbol{V}^*. \tag{A 8}$$

Equations (A 7) and (A 8) show that the inner flow problem is characterized by a modified Reynolds number $Re_M = ReR_c/c$, which is based on nose radius of curvature and is much smaller than Re. In this way, the local viscous effects around the aerofoil nose are correctly accounted for, specifically when the flow tends to separate and indicate the onset of stall. Moreover, in the inner region, to leading order, the aerofoil is described by a canonic smooth parabola $y^* = \pm\sqrt{2x^*}$ (which sets the radius of curvature to unity). Along the parabola's upper and lower surfaces the no-penetration and no-slip conditions are satisfied. In the far field of the inner region the flow is steady and viscous effects are negligible. The velocity potential Φ^*, where $\boldsymbol{V}^* = \boldsymbol{\nabla}\Phi^*$, is scaled with $U_\infty R_c$ and in the far field of the inner region (Rusak 1994) is given by

$$\frac{\Phi}{U_\infty R_c} = \Phi^* \approx x^* + \sqrt{2r^*}\sin\frac{\theta^*}{2} + \tilde{A}\sqrt{2r^*}\cos\frac{\theta^*}{2} + O(\log r^*, \theta^*). \tag{A 9}$$

Here, $r^* = \sqrt{x^{*2} + y^{*2}} \to \infty$ and $\theta^* = \arctan(y^*/x^*)$. Equation (A 9) shows that the inner-region far-field flow is near uniform and with higher-order correction terms that relate to a symmetric flow due to the symmetric nose curvature and an asymmetric

circulatory flow with the circulation parameter $\tilde{A}$. Equations (A 7), (A 8) and (A 9) show that in the inner region, the flow is governed by the modified Reynolds number Re_M and the circulation parameter $\tilde{A}$, which is determined by the matching process in the following section. The parameter $\tilde{A}$ is directly associated with the pressure distribution and its gradient, and thereby affects the boundary-layer behaviour along the parabola surface.

A.3. *Matching*

The matching of the inner and the outer regions is established in an overlap region between them and outside the thin boundary layer, where the flow is dominated by inviscid effects. The matching is carried out with the help of an intermediate overlap region $\eta(\delta)$, where $r_\eta = \bar{r}/\eta(\delta)$ held fixed in the limit $\delta \to 0$ and $\delta^2 \ll \eta(\delta) \ll 1$. Then as $\delta \to 0$, $\eta(\delta)/\delta^2 \to \infty$, $\bar{r} = r_\eta \eta(\delta) \to 0$ and $r^* = \eta r_\eta/(2h^2\delta^2) \to \infty$. The parameter $\eta(\delta)$ represents a whole order-class of limits between the inner and the outer regions, where $\eta(\delta) = \delta^k$ and k is between 0 and 2. For matching, the expansions in (A 5) and (A 9) must read the same up to a certain order when expressed in terms of r_η and $\theta^* = \theta$, as follows. Outer:

$$\begin{aligned}\Phi &= \bar{\Phi} U_\infty c \\ &\approx U_\infty c \left[\frac{x}{c} + \delta\left(2h\sqrt{r_\eta \eta}\sin\frac{\theta}{2} + 2Aw_0\sqrt{r_\eta\eta}\cos\frac{\theta}{2}\right) + O(r_\eta\eta\log r_\eta\eta, r_\eta\eta)\right]. \quad \text{(A 10)}\end{aligned}$$

Inner:

$$\begin{aligned}\Phi &= \Phi^* U_\infty R_c \\ &\approx U_\infty R_c\left(\frac{x}{R_c} + \sqrt{\frac{2\eta r_\eta}{2h^2\delta^2}}\sin\frac{\theta}{2} + \tilde{A}\sqrt{\frac{2\eta r_\eta}{2h^2\delta^2}}\cos\frac{\theta}{2} + O\left(\log\frac{2\eta r_\eta}{2h^2\delta^2}, \theta\right)\right) \\ &= U_\infty c\left(\frac{x}{c} + 2h\delta\sqrt{\eta r_\eta}\sin\frac{\theta}{2} + 2h\delta\tilde{A}\sqrt{\eta r_\eta}\cos\frac{\theta}{2} + O\left(\log\frac{2\eta r_\eta}{2h^2\delta^2}, \theta\right)\right). \quad \text{(A 11)}\end{aligned}$$

The matching between (A 10) and (A 11) yields $2h\delta\tilde{A} = 2Aw_0\delta$ or $\tilde{A} = Aw_0/h$.

REFERENCES

ABBOTT, I. H. & VON DOENHOFF, A. E. 1958 *Theory of Wing Sections*, 2nd edn. Dover.

ANDERSON, J. D. JR 2007 *Fundamentals of Aerodynamics*, 4th edn. McGraw-Hill.

BATCHELOR, G. K 1967 *An Introduction to Fluid Dynamics*. Cambridge University Press.

BHASKARAN, R. & ROTHMAYER, A. P. 1998 Separation and instabilities in the viscous flow over airfoil leading edges. *Comput. Fluids* **27** (8), 903–921.

CARR, L. W. 1988 Progress in analysis and prediction of dynamic stall. *J. Aircraft* **25** (1), 6–17.

CEBECI, T., KHATTAB, A. K. & STEWARTSON, K. 1980 On nose separation. *J. Fluid Mech.* **97**, 435–454.

CHENG, H. K. & SMITH, F. T. 1982 The influence of airfoil thickness and Reynolds number on separation. *J. Appl. Math. Phys. (Z. Angew. Math. Phys.)* **33**, 151–180.

VAN DOMMELEN, L. L. & SHEN, S. F. 1980 The spontaneous generation of the singularity in a separating laminar boundary layer. *J. Comput. Phys.* **38** (2), 125–140.

ELLIOTT, J. W. & SMITH, F. T. 1987 Dynamic stall due to unsteady marginal separation. *J. Fluid Mech.* **179**, 489–512.

GAULT, D. E. 1957 A correlation of low-speed, airfoil-section stalling characteristics with Reynolds number and airfoil geometry. NACA TN 3963.

GROVE, D. V., LAIOSA, J. P., WOODSON, S. H. & STOOKESBERRY, D. C. 2002 Computational fluid dynamics study of an abrupt wing stall phenomena on the F/A-18E. *AIAA Paper* 2002-1025.

HOFFMANN, K. A. & CHIANG, S. T. 1993 *Computational Fluid Dynamics for Engineers*. Engineering Education System.

JACOBS, E. N. & SHERMAN, A. 1937 Airfoil section characteristics as affected by variations of the Reynolds number. NACA Report 586.

JONES, B. M. 1934 Stalling. *J. R. Aero Soc.* **38**, 753–770.

KUNZ, P. J. & KROO, I. 2001 Analysis and design of airfoils for use at ultra-low Reynolds numbers. In *Fixed and Flapping Wing Aerodynamics for Micro Air Vehicle Applications* (ed. T. J. Muller), Prog. in Astronautics and Aeronautics, vol. 195, AIAA.

LIEBECK, R. H. 1973 A class of airfoils designed for high lift in incompressible flow. *J. Aircraft* **10** (10), 610–617.

MCCORMICK, B. W. 1995 *Aerodynamics, Aeronautics and Flight Mechanics*, 2nd edn. Wiley.

MORRIS, W. J. II 2009 A universal prediction of stall onset for airfoils over a wide range of Reynolds number flows. PhD thesis, Rensselaer Polytechnic Institute, Troy, NY.

NAKAYAMA, Y. 1988 *Visualized Flow*. Pergamon.

PAVELKA, J. & TATUM, K. 1981 Validation of a wing leading-edge stall prediction technique. *J. Aircraft* **18** (10), 849–854.

PINIER, J. T., AUSSEUR, J. M., GLAUSER, M. N. & HIGUCHI, H. 2007 Proportional closed-loop feedback control of flow separation. *AIAA J.* **45** (1), 181–190.

ROACHE, P. J. 1998 *Fundamentals of Computational Fluid Dynamics*. Hermosa.

RUBAN, A. I. 1982 Asymptotic theory of short separation bubbles at the leading edge of a thin airfoil. *Izv. Akad. Nauk SSSR Mekh. Zhidk. Gaza* (1), 42–52.

RUSAK, Z. 1994 Subsonic flow around the leading edge of a thin aerofoil with a parabolic nose. *Eur. J. Appl. Maths* **5**, 283–311.

RUSAK, Z. & MORRIS, W. J. II 2011 Stall onset on airfoils at moderately high to high Reynolds number flows. *Trans. ASME: J. Fluids Engng* **133** (11), 111104.

SELIG, M. S., LYON, C. A., GIGUERE, P., NINHAM, C. P. & GUGLIELMO, J. J. 1996 Summary of low-speed airfoil data, vol. 2. Department of Aero. & Astro. Engineering, University of Illinois at Urbana-Champaign.

SOUSA, E. 2003 The controversial stability analysis. *Appl. Maths Comput.* **145** (2/3), 777–794.

STEWARTSON, K., SMITH, F. T. & KAUPS, K. 1982 Marginal separation. *Stud. Appl. Maths* **67** (1), 45–61.

SYCHEV, V. V., RUBAN, A. I., SYCHEV, V. V. & KOROLEV, G. L. 1998 *Asymptotic Theory of Separated Flows*. Cambridge University Press.

TANI, I. 1964 Low speed flows involving bubble separations. *Prog. Aerosp. Sci.* **5**, 70–103.

THOMPSON, H. D., WEBB, B. W. & HOFFMAN, J. D. 1985 The cell Reynolds number myth. *Intl J. Numer. Meth. Fluids* **5**, 305–310.

WEBSTER, B. E., SHEPHARD, M. S., RUSAK, Z. & FLAHERTY, J. E. 1994 Automated adaptive time-discontinuous finite-element method for unsteady compressible aerofoil aerodynamics. *AIAA J.* **32** (4), 748–757.

WERLE, M. J. & DAVIS, R. T. 1972 Incompressible laminar boundary layers on a parabola at angle of attack: a study of the separation point. *Trans. ASME: J. Appl. Mech.* **39** (1), 7–12.

YEN, S. C. & HUANG, L.-C. 2009 Flow patterns and aerodynamic performance of unswept and swept-back wings. *Trans. ASME: J. Fluids Engng* **131** (11) 111101.